University of Tartu

Faculty of Science and Technology

Institute of Ecology and Earth Sciences

Department of Geology

Alvar Ratt

Composition of magnetite trace elements in the Jõhvi magnetic quartzite in north-east Estonia as an indicator of iron mineralisation processes

Master's thesis in Geology (30 EAP)

Supervisor:

Kalle Kirsimäe

Siim Nirgi

Tartu 2024

Composition of magnetite trace elements in the Jõhvi magnetic quartzite in north-east Estonia as an indicator of iron mineralisation processes

The aim of this master's thesis was to study the origin of the iron mineralisation in the crystalline basement from the Jõhvi magnetic anomaly, Estonia, using the geochemical analysis of the magnetite trace elements. Magnetite-bearing samples from the magnetite mineralisation intervals of drill cores PA-1 and PA-2 were described petrographically, and the trace element composition of the magnetite was characterised by using analytical scanning electron microscopy and laser ablation inductively coupled plasma mass spectrometry. The results of this study show that magnetite divides into different types depending on the host rock mineral composition. Compared to the previous studies on magnetite trace-element composition from various iron ore deposits, the initial origin of Jõhvi magnetite mineralization was most likely related to the formation of the banded iron formation (BIF). However, the trace-element composition of the magnetite has been changed due to orogenetic granulite facies regional metamorphism and alteration by hydrothermal fluids.

Keywords: magnetite, trace elements
CERS code: P420 petrology, mineralogy, geochemistry

Magnetiidi jälgelemendid raua maagistumise protsesside indikaatorina Kirde-Eesti Jõhvi magnetkvartsiitides

Käesoleva magistritöö eesmärk oli selgitada mikroelementide geokeemilise analüüsi abil rauamineralisatsiooni päritolu Jõhvi magnetilise anomaaliat põhjustavates raud-kvartsiitides. Puursüdamike PA-1 ja PA-2 magnetiiti kandvatest intervallidest võetud proove kirjeldati petrograafiliselt ning magnetiidi mikroelementide koostist iseloomustati analüütilise skaneeriva elektronmikroskoopia ja laserablatsiooni induktiivselt sidestatud plasma massispektromeetria abil. Uuringu tulemused näitavad, et magnetiit jaguneb erinevateks tüüpideks lähtuvalt ümbriskivimi mineraloogilisest koostisest. Jõhvi magnetilise anomaalia magnetiit oli suure tõenäosusega algselt seotud settelise raua ladestu (banded iron formation - BIF) tekkega, kuigi magnetiidi jälgelementide koostis on muutunud hilisema orogeense granuliitse faatsiese regionaalmetamorfismi käigus ja hüdrotermaalsete fluidide mõjul.

Märksõnad: Jõhvi magnetiline anomaalia, magnetiit, jälgelemendid

CERS kood: P420 petroloogia, mineraloogia, geokeemia

Table of contents

Introduction

Jõhvi Magnetic Anomaly (JMA) was discovered nearly a hundred years ago in the early 1930s. It is the first and the strongest (19300 nT; Plado et al., 2020) of several strong isolated magnetic anomalies in the Estonian crystalline basement (Figure 1). Detailed geophysical mapping and the first drilling campaign of the anomaly were undertaken between 1935 and 1939, resulting in two deep drill holes (Jõhvi-I and Jõhvi-II) that intersected magnetite quartzite rocks in the crystalline basement causing the magnetic anomaly (Linari, 1940). Geological exploration of the JMA continued in the 1960s with additional gravimetric and magnetometric mapping in 1961 and 1964–1965, along with further drilling in 1967–1968 (Suuroja, 1969; Erisalu & Arvisto, 1969; Nirgi et al., 2022).

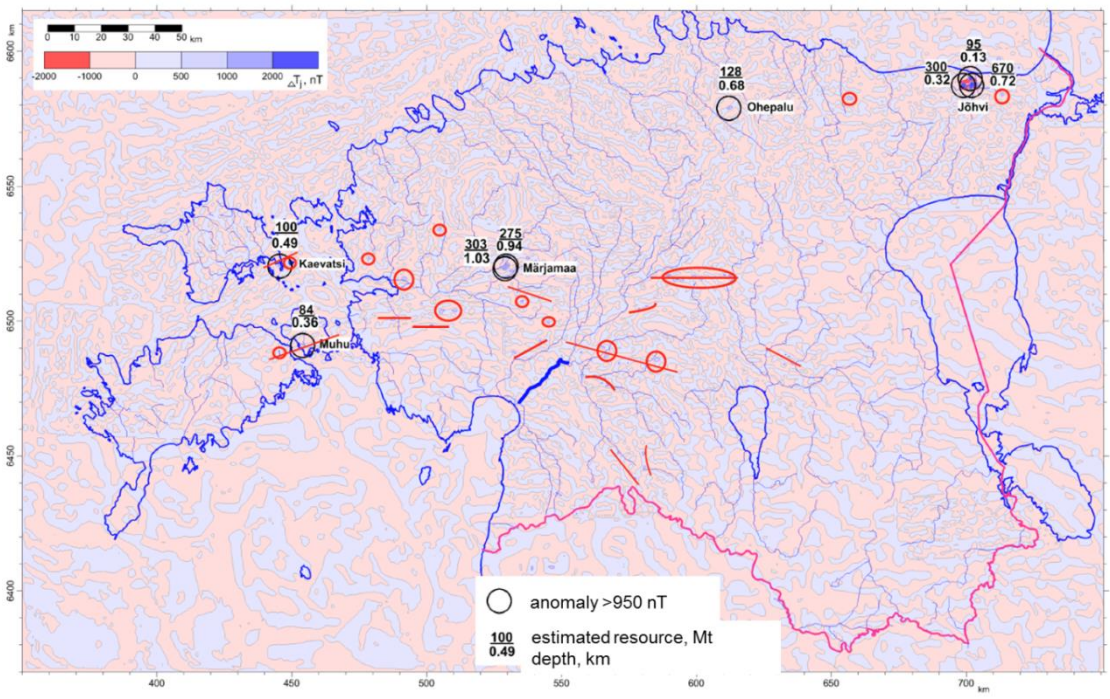

Figure 1. Map of the residual anomalies of the magnetic field of Estonian territory with the main magnetic anomalies and their potential magnetite resource and the estimated depth of the rock body centre. Compiled by M. Shtokalenko, Estonian Geological Survey (2021).

The investigation of the JMA resumed in 2019 when the Geological Survey of Estonia drilled two 770 m deep inclined diamond core boreholes in the Jõhvi Magnetic Anomaly area. This new drilling aimed to estimate the exploration potential of iron mineralization and to investigate the presence of other mineralization types (Nirgi et al., 2022). Studies of the new cores confirmed the main results of earlier studies, indicating that the Jõhvi Magnetite Anomaly is caused by sub-

vertical, partially mineralized metamorphic rocks rich in magnetite in the crystalline basement beneath the 240 m sedimentary cover that possibly extends to the depth of 1000 m.

In addition to magnetite quartzites and magnetite-rich gneisses, sulphide, and magnetite-sulphide mineralization intervals occur. Sulphide mineralization is predominantly represented by pyrrhotite, with lesser amounts of pyrite and chalcopyrite. The presence of sulphide mineralization was noted during earlier investigations of the JMA, with reported Cu levels up to 0.7 wt% (Luha, 1946) and Zn levels at 0.42 wt% (Linari, 1940). Recent investigations have indicated limited Cu-Zn mineralization in the JMA (Nirgi et al., 2022). However, rare arsenopyrite and löllingite were identified during core logging of the latest drill cores PA-1 and PA-2, suggesting high-temperature hydrothermal processes in the JMA (Nirgi et al., 2022). Different sulphide generations, including hydrothermal pyrites, were confirmed by trace elements study of pyrite and pyrrhotite by Ratt (2022).

Soesoo et al. (2021) conducted a study on the petrography and geochemistry of the Jõhvi magnetite quartzites, showing that magnetite-bearing beds occur as sub-vertical beds with complicated structural elements in garnet-cordierite and pyroxene gneisses. Magnetite quartzites exhibit a wide range of major element compositions, with unusually high manganese content (1–6 wt%). While most of the magnetite quartzites followed a similar rare earth element (REE) pattern to the surrounding gneisses, granitoids showed significantly different REE patterns (Soesoo et al., 2021). Soesoo et al. (2021) also noted from a limited number of *in-situ* trace element analyses of magnetite that the results from drill core J-1 were unambiguous in classifying Jõhvi magnetite into a certain deposit type and the origin of JMA iron-ore remains unclear.

This thesis focuses on the trace element analysis of JMA magnetite in iron-ore-bearing intervals in drill cores PA-1 and PA-2- aiming to reveal the magnetite mineralization type of the JMA magnetite ores.

Geological Setting

The Paleo- to Mesoproterozoic crystalline bedrock of Estonia primarily comprises the Svecofennian metamorphic and plutonic formations, alongside anorogenic plutonic rapakivi granites, which cut through the Svecofennian metamorphic complex (Puura et al., 1996). This bedrock, which is structurally akin to the Svecofennian Domain of the Fennoscandian Shield has a flat peneplaned erosional surface dipping approximately 2 to 4 meters per kilometre towards the south and is buried under a sedimentary sequence ranging from around 100 meters in northern Estonia to roughly 800 meters in thickness in southern and southwestern Estonia so that there are no crystalline basement outcrops in the Estonian mainland.

Structurally, the Estonian crystalline basement is typified by two principal units - the northern section dominated by amphibolite facies metamorphic rocks, while the southern region features metamorphic rocks ascending to the granulite facies (Puura et al., 1996; Soesoo et al., 2004). These metamorphic zones are further delineated into six distinct zones (Figure 2) based on their petrological and geophysical attributes, namely the Tallinn, Alutaguse, Tapa, West Estonian, South Estonian, and Jõhvi Zones. According to Puura et al. (1996) and Soesoo et al. (2004, 2020), the Tallinn Zone is characterized by a variety of metamorphic rocks, including amphibole gneisses, biotite-plagioclase gneisses, quartz-feldspar gneisses, mica gneisses, sulphide-graphite gneisses, and magnetite quartzites, all belonging to the amphibolite facies. The Alutaguse Zone is primarily distinguished by Al-rich gneisses, biotite-plagioclase gneisses, along with some amphibole gneisses, amphibolites, and quartz-feldspar gneisses, all within the amphibolite facies. In contrast, the Tapa Zone is typified by garnet and pyroxene quartzites, Al (garnet-cordierite-sillimanite) gneisses, and pyroxene-, amphibole-, and biotite-rich gneisses of varying metamorphic grades ranging between amphibolite and granulite facies. The West Estonian Zone predominantly comprises metasedimentary amphibolites, biotite-plagioclase gneisses, and quartz-feldspar gneisses, transitioning from amphibolite to granulite facies. The South Estonian Zone, meanwhile, primarily features metamorphosed volcanic rocks, attaining granulite facies metamorphism, notably amphibole-pyroxene and biotite-pyroxene gneisses, alongside quartz-feldspar gneisses.

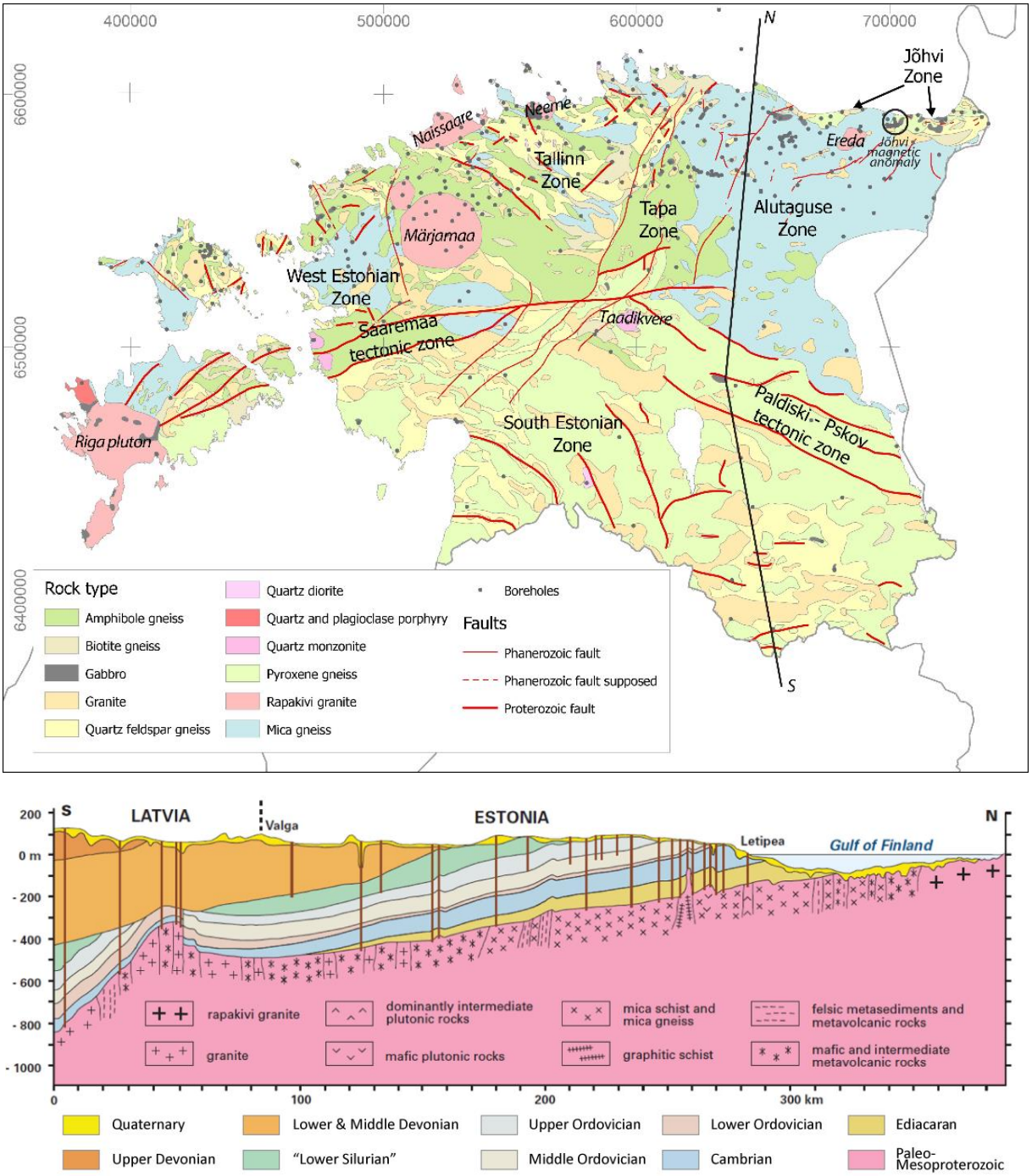

Figure 2. Geological map of the Estonian crystalline basement (Koppelmaa, 2002) and cross-section of the sedimentary cover and crystalline basement along the N-S (Modified after Vaher et al., 1962)

The Jõhvi Zone, where the Jõhvi Magnetic Anomaly (JMA) is situated, forms a narrow belt spanning 20 to 30 kilometres in width and extending approximately 100 kilometres within the amphibolite grade gneisses of the Alutaguse Zone in northeastern Estonia. Crystalline formations within the Jõhvi Zone are characterized by migmatised gneisses/granites of diverse compositions, encompassing pyroxene gneisses, quartz-feldspar gneisses, biotite-plagioclase gneisses,

amphibole gneisses, garnet-cordierite gneisses, collectively referred to as the Vaivara complex, and magnetite-rich gneisses/quartzites. According to Soesoo et al. (2021) these rocks have undergone granulite facies metamorphism, with the bedding of gneisses and magnetite-bearing quartzites exhibiting a sub-vertical orientation. The magnetite-rich gneisses/quartzites manifest as sub-vertical beds within garnet-cordierite or pyroxene gneisses, interspersed with numerous migmatite granites exhibiting variable apparent thicknesses of up to 34.6 meters. The magnetic anomaly attributed to the magnetite-rich rocks is characterized by several anomaly maxima reaching up to 19300 nT within the so-called western anomaly, accompanied by slight positive gravity anomalies (Plado et al., 2020). The mineralized zones within the JMA rocks predominantly comprise magnetite and/or magnetite-sulphide mineralization, with drill cores PA-1 and PA-2 exhibiting a total apparent thickness of mineralized intervals exceeding 100 meters (Nirgi et al., 2022). The individual thickness of separate magnetite-rich mineralization intervals varies from 0.12 to 50.0 meters, while intervals containing magnetite-sulphide mineralization range from 0.20 to 30.85 meters in thickness (Nirgi et al., 2021).

Trace elements in magnetite

Magnetite (Fe_3O_4) forms through a variety of geological processes, including magmatic crystallization, hydrothermal alteration, metamorphism, and weathering. In magmatic settings, magnetite can crystallize from magma or differentiate from ferromagnesian minerals. Hydrothermal fluids can also precipitate magnetite in veins and replacement deposits. Metamorphic processes can alter pre-existing minerals to form magnetite, while weathering of iron-bearing minerals can lead to the formation of secondary magnetite. (Dupuis & Beaudoin, 2011)

Through those different geological processes, magnetite could be found in many classified mineral deposit types: iron oxide-copper-gold (IOCG), Kiruna apatite-magnetite, banded iron formation (BIF), porphyry Cu, Fe-Cu skarn, Fe-Ti, V, Cr, Ni-Cu-PGE, Cu-Zn-Pb volcanogenic massive sulfide (VMS), Archean Au-Cu porphyry, and Opemiska type Cu veins. In IOCG deposits magnetite occurs as a primary mineral or as an alteration product (Skirrow, 2022). IOCG deposits are characterized by the presence of iron oxide minerals, copper, gold, and other elements, and magnetite is a key indicator mineral in these systems. BIF deposits are probably the most common and abundant occurrences of magnetite. These deposits consist of alternating layers of iron-rich minerals, including magnetite and hematite, and are important sources of iron ore (Klein, 2005). Magnetite can also be present in porphyry Cu deposits, where it may occur as a primary mineral or as an alteration product associated with hydrothermal activity. VMS deposits can contain magnetite as a minor accessory mineral, often associated with base metal sulfides such as Cu, Zn, and Pb (Yildirim et al., 2016). Skarn deposits can host magnetite as a result of contact metamorphism and metasomatic processes involving the interaction of hydrothermal fluids with carbonate rocks (Mao et al. 2005). Magnetite can be found in hydrothermal vein deposits associated with a variety of mineralization styles, including Au, Ag, Cu, and base metals (Nadoll et al., 2014). Magnetite is also a common accessory mineral in metamorphic rocks, where it can form through the alteration of pre-existing minerals under high-temperature and pressure conditions (Jafari et al., 2019).

Magnetite can incorporate various trace elements through solid solution substitutions and crystal growth processes whereas the most common trace elements found in magnetite include Mg, Mn, Zn, V, Co, Cr, Ni, and REEs (Dupuis & Beaudoin, 2011). The trace element composition of the magnetite is a fingerprint of its physical-chemical formation environment

and can be used to decipher different magnetite ore genetic types. Dupuis & Beaudoin (2011) have suggested that the Ni+Cr vs. Si+Mg diagram can be used to isolate Ni-Cu-PGE, and Cr deposits from other deposit types. The Al/(Zn+Ca) vs. Cu/(Si+Ca) diagram can be used to separate Cu-Zn-Pb VMS deposits. Samples plotting outside the Ni-Cu-PGE and Cu-Zn-Pb VMS fields can be discriminated using the Ni/(Cr+Mn) vs. Ti+V or Ca+Al+Mn vs. Ti+V diagrams to assign magnetite mineralisation to either IOCG, Kiruna, porphyry Cu, BIF, skarn, and/or Fe-Ti and/ V deposits. This method has been widely used in defining iron-ore origin by magnetite trace-element composition.

Material and Methods

In this study, 17 samples were chosen from the geological survey of drill cores PA-1 and PA-2 (Table 1, Figure 3), which represent different mineralised zones intersected in cores.

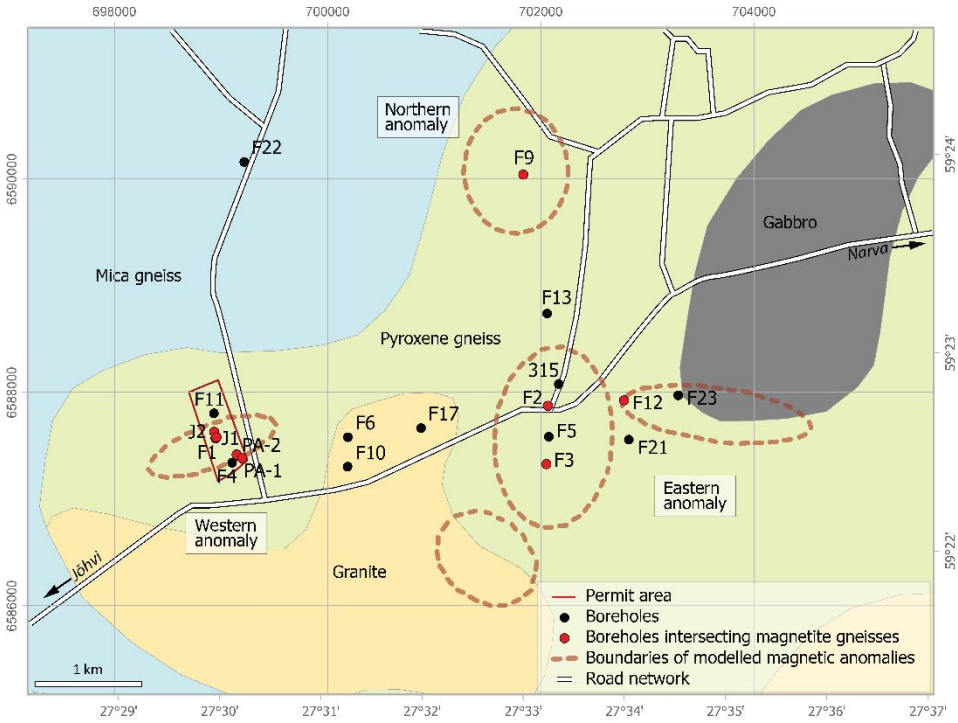

Figure 3. Geological map of the crystalline basement of the Jõhvi Magnetic Anomaly with modelled boundaries of single iron ore bodies and locations of deep boreholes in the area together with studied PA-1 and PA-2 on the Western anomaly (from Nirgi et al., 2022; after Koppelmaa, 2002 and Plado et al., 2021).

Ten samples were made into thin sections, and seven were thick sections. Six samples are from drill core PA-1 and eleven samples are from drill core PA-2 (Figure 4).

Thin sections were inspected and photographed under the binocular and optical polarizing microscope in transmitted and reflected light, and in scanning electron microscope using back-scattered electron (BSE) imaging with ZEISS EVO MA15 SEM equipped with Oxford AZTEC-MAX energy-dispersive (EDS) system.

Trace element concentration measurements were performed with laser ablation inductively coupled plasma mass spectrometry (LA-ICP-MS) using an Agilent 8800 quadrupole ICP-MS coupled to a Cetac LSX- 213 G2+ laser with HelEx II fast-washout two-volume large-format

cell and ‘Squid’ smoothing interface at University of Tartu.

Table 1. Host-rock types of the analysed magnetite grains. Feldspar (Fsp), Garnet (Grt), Pyroxene (Px), Biotite (Bt), Plagioclase (Pl), Amphibole (Amp), Kfs (K-feldspar), Pyrite (Py), Pyrrhotite (Po), Chlorite (Chl).

Sample ID	**Borehole**	**Depth**	**Mineralogy***	**Group**	**No of grains**
J-PA1-2	PA1	726.46	Pl-Bt-Px	Fsp	4
TS-00024	PA2	736.79	Grt-Fsp	Fsp	12
TS-00025	PA1	317.4	Kfs-Bt-Pl	Fsp	7
TS-00027	PA1	343.68	Kfs-Pl-Bt	Fsp	6
J-PA2-2	PA2	562.05	Grt-Bt	Grt	4
TS-00035	PA1	561.97	Pl-Amp-Bt-Grt	Grt	7
TS-00036	PA2	562.14	Grt-Bt	Grt	9
TS-00010	PA2	447.32	Grt-Py-Po-Chl	Grt2	6
J-PA1-1	PA1	511	Px-Grt	Grt-Px	5
PA2-10s	PA2	497.75	Px-Grt	Grt-Px	2
PA2-11s	PA2	593.3	Px-Grt	Grt-Px	4
TS-00011	PA2	455.32	Px-Grt	Grt-Px	12
J-PA2-1	PA2	474.68	Pl-Px-Amp-Grt	Grt-Px-Pl	6
TS-00033	PA1	456.88	Pl-Kfs-Bt	Pl	9
PA2-SEM8	PA2	629	Amp-Px	Px-Amp	3
TS-00019	PA2	629.82	Amp-Px	Px-Amp	11
TS-00021	PA2	678.73	Amp-Px	Px-Amp	8

*in decreasing abundance

Spot analysis on the samples was performed using the following laser parameters: fluence 3.2J/cm^2, repetition rate 10 Hz, 50 μm round spot. 20 s of gas blank were collected before each ablation pass and ablation signal was collected for 45s. USGS GSD1G and MASS1 were used as the calibration standards and were measured in triplicates after 20 samples ablations. The oxide formation ratio expressed as ThO/Th from ablation of NIST 610 during instrument tuning was <0.25%.

Signals of ^{24}Mg, ^{27}Al, ^{28}Si, ^{29}Si, ^{31}P, ^{39}K, ^{43}Ca, ^{47}Ti, ^{49}Ti, ^{51}V, ^{52}Cr, ^{55}Mn, ^{59}Co, ^{60}Ni, ^{66}Zn, ^{71}Ga, ^{72}Ge, ^{73}Ge, ^{90}Zr, ^{93}Nb, ^{95}Mo, ^{107}Ag, ^{118}Sn, ^{178}Hf, ^{181}Ta, ^{182}W were collected with a dwell time of 6 ms, ^{63}Cu, ^{209}Bi with a dwell timeof 10 ms and ^{208}Pb was collected with a dwell time of 20 ms, surmounting to a total duty cycle of 0.33 s on the ICP-MS.

Data reduction of the raw signals was performed using Iolite V4. After background substitution the X-Trace_Elements IS data reduction scheme with quantitative standardisation method using Fe as an internal standard element was used for concentration calculations. GSD1G standard was used as the calibration standard for all elements. For magnetite samples, a stoichiometric Fe concentration in magnetite of 72.36 % was used as an internal standard value.

Because of numerous silicate and other mineral impurities/inclusions that were not identified prior to analysis, the LA-ICP-MS raw datawere filtered and the data where K content was over 500 ppm, and where both Ca and Al were over 1000 ppm were excluded from further analysis. Median values of each analysed element were used from multiple measurement points of the same grain. Altogether data from 115 magnetite grains were analysed.

Principal component analysis (PCA) of magnetite trace-element data was performed using CoDaPack code that performs prior PC-analysis a log-ratio transformation of the data to open the otherwise closed compositional data sets (Aitchison et al. 2000).

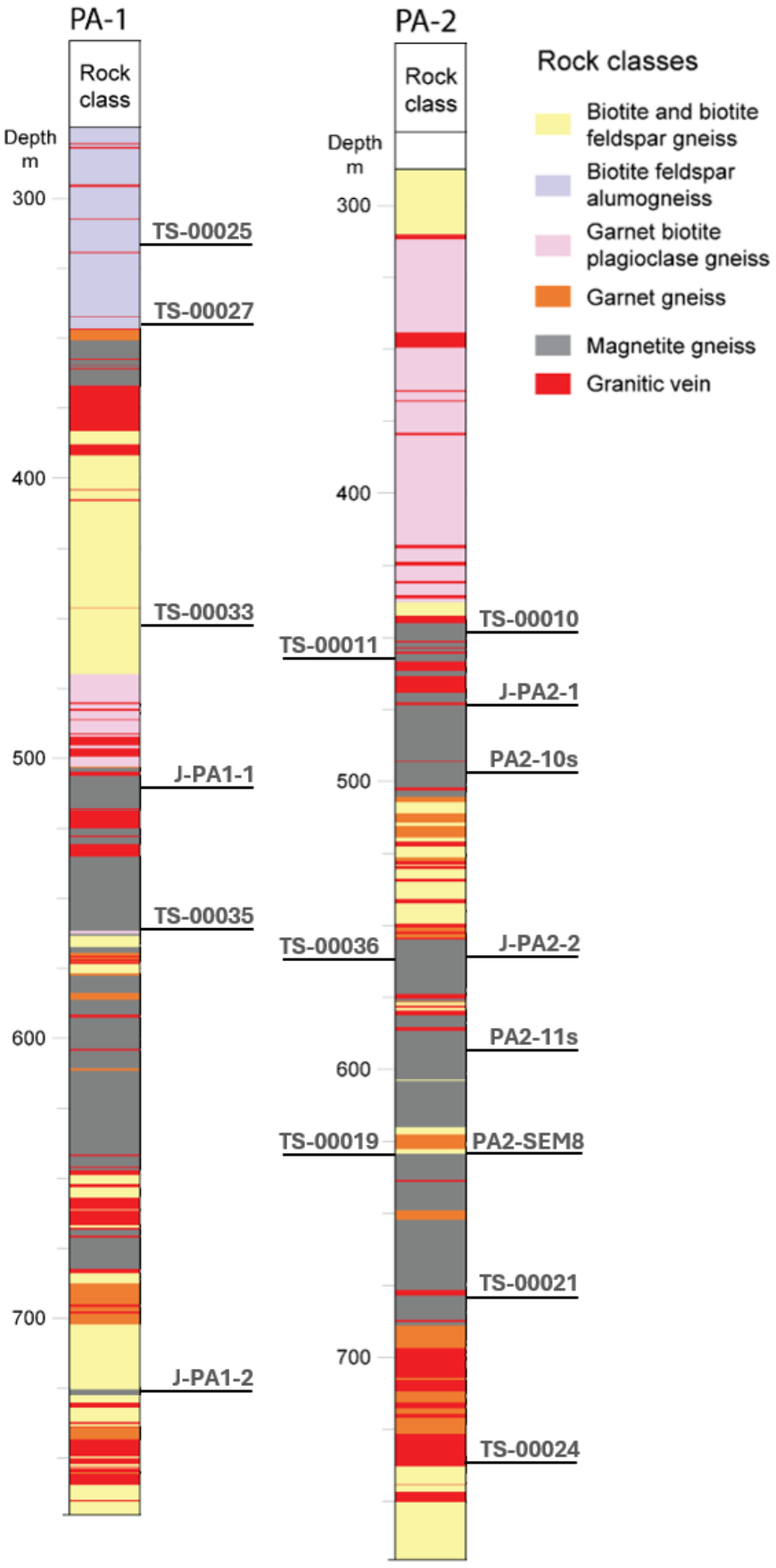

Figure 4. Schematic drillhole profiles of PA-1 and PA-2 with rock classes described in Nirgi et al. (2022) with the locations of the studied samples.

Results

Sample Petrography

Magnetite mineralisation in JMA drill cores PA-1 and PA-2 is characterised by magnetite xenoblastic grains that mainly occur as 1-3 mm directional and elongated grains (Figure 5). Magnetite grains can also form massive aggregates, or occurs as separate and rounded xenoblastic grains (Figure 6).

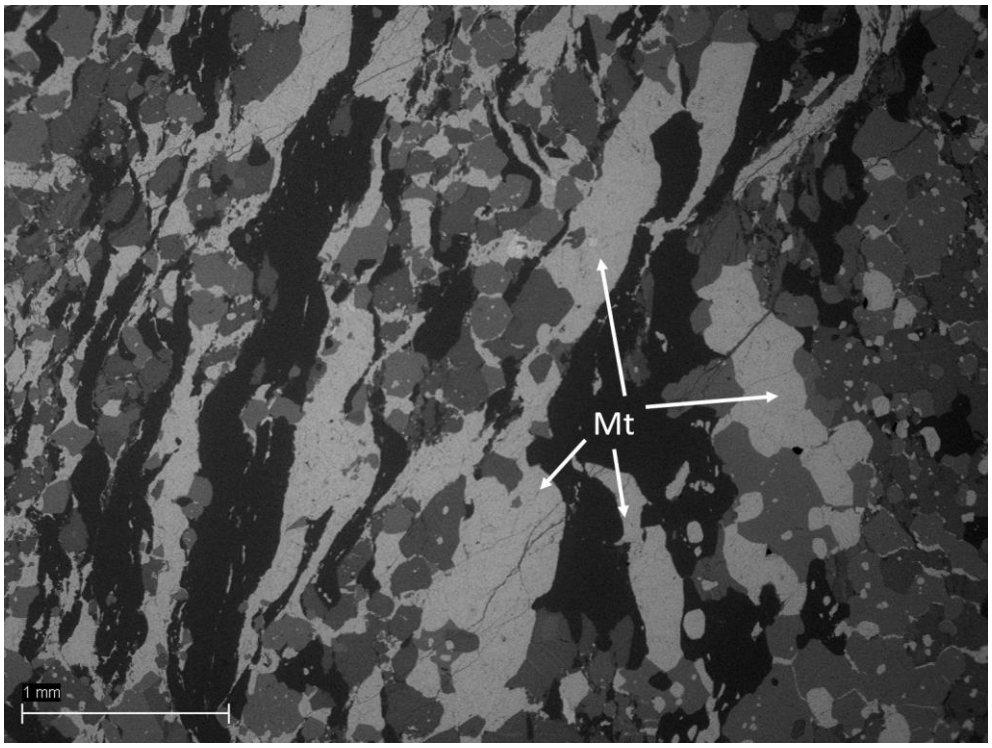

Figure 5. Backscattered scanning electron (BSE) microscope image of the magnetite (Mt) xenoblastic grains in garnet magnetite gneisses. PA-2 core, sample TS-00036, depth 562,14 m.

In andalusite and/or sillimanite-cordierite bearing biotite feldspar gneissic host rocks, the magnetite occurs as mesoblastic elongated grains, reaching lengths of up to 1.5 millimetres that are aligned parallel to the rock's fabric, particularly within layers with abundant in sillimanite. A similar magnetite texture is in magnetite garnet biotite amphibole plagioclase gneisses where magnetite occurs with sulphide and in chlorite-bearing magnetite garnet gneiss, and garnet magnetite pyroxene gneiss (Figure 7). In the latter, the magnetite is found as xenoblastic grains, frequently elongated and aligning preferentially with the rock fabric, displaying irregular shapes amidst silicate minerals. Magnetite tends to segregate into discrete

bands of heightened magnetite concentration, particularly prevalent within a 10-millimeter-wide band where it is partly interspersed or embedded within other minerals in a skeletal manner (Figure 8).

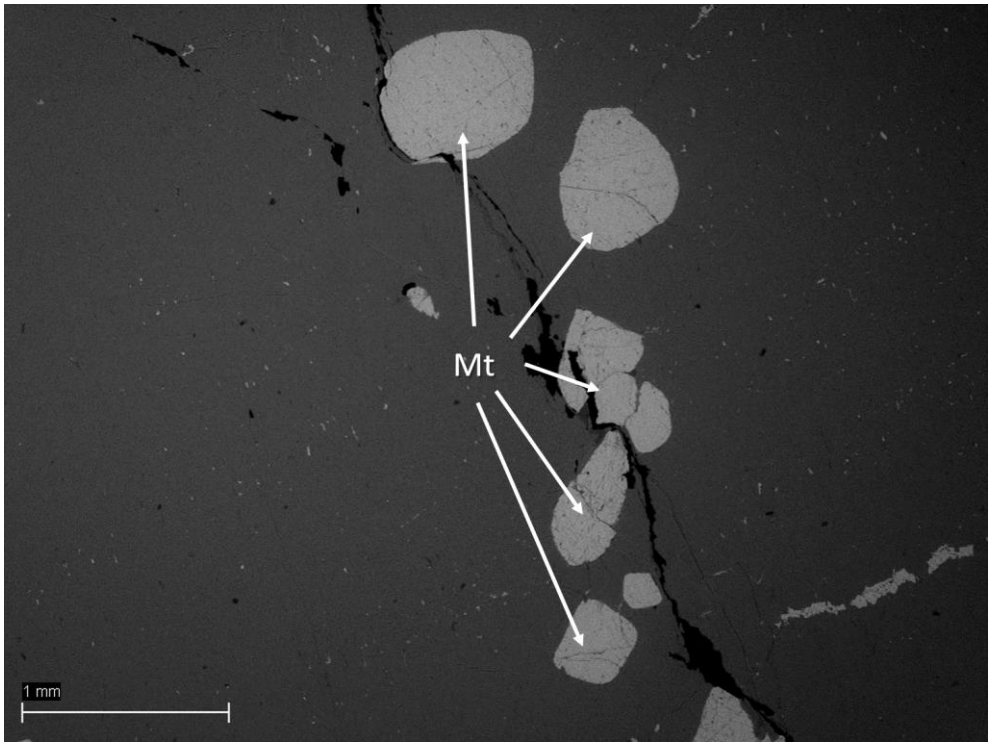

Figure 6. BSE microscope image of the magnetite (Mt) rounded xenoblastic grains in biotite-bearing amphibole magnetite gneisses. PA-2 drill core, sample TS-00019, depth 629.82 m.

In pyroxene amphibole magnetite gneisses, the magnetite is the dominant mineral with elongated fabric, whereas magnetite is predominantly found alongside pyroxene and is often enclosed within it within domains dominated by magnetite and pyroxene (Figure 8).

Based on the mineralogical composition of the magnetite-bearing host rocks the magnetite samples were divided into seven groups: Feldspar (Fsp), Garnet (Grt), Garnet2 (Grt2), Garnet-Pyroxene (Grt-Px), Garnet-Pyroxene-Plagioclase (Grt-Py-Pl), Plagioclase (Pl), and Pyroxene-Amphibole (Px-Amp) host rock types.

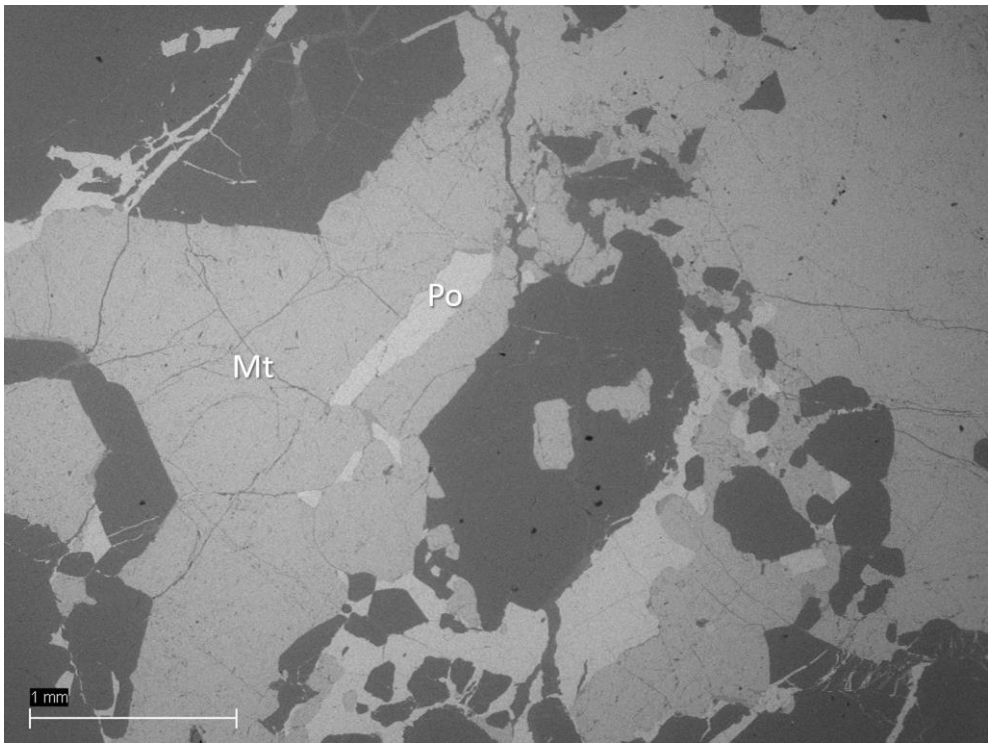

Figure 7. BSE microscope image of the magnetite (Mt) with pyrrhotite (Po) inclusion in chlorite-bearing magnetite garnet gneisses. PA-2 drill core, sample TS-00010, depth 447,32 m.

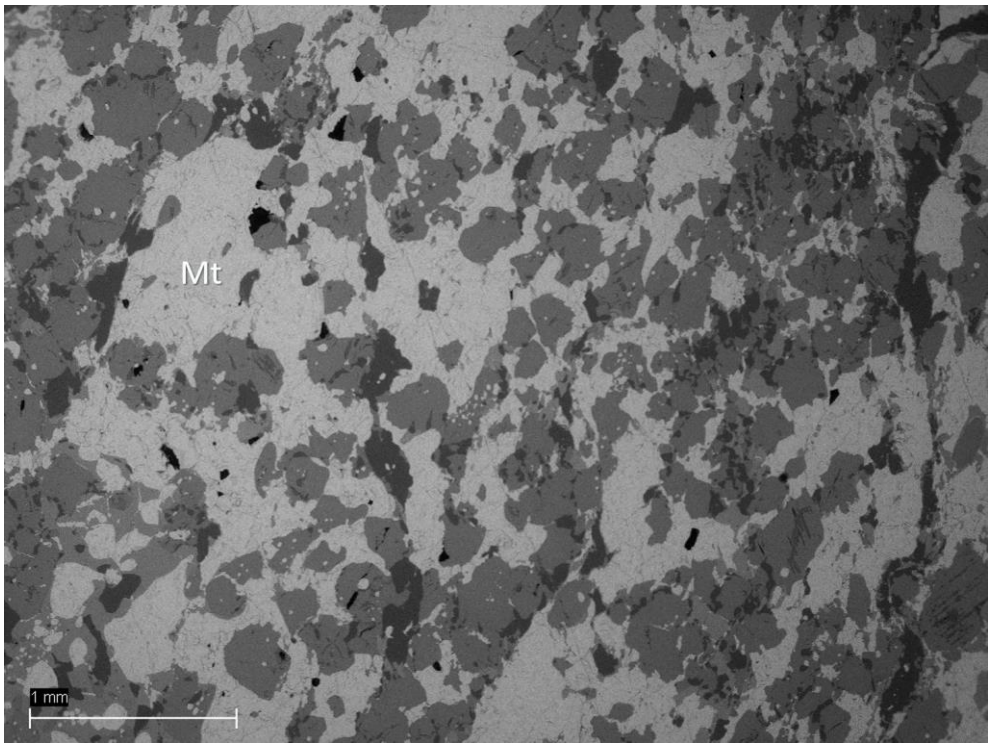

Figure 8. Backscattered scanning electron microscope image of the part of 10-millimeter-wide magnetite (Mt) band in garnet magnetite pyroxene gneisses. PA-2 drill core, sample TS-00011, depth 455,32 m.

Magnetite Trace Element Composition

The trace element composition of the magnetite in studied JMA samples is shown in Figure 9 and Appendix 1. The most abundant trace elements in JMA magnetites are V, Cr, Ni, Ti and Mn. Their content in JMA magnetite shows high variability. The V content ranges in samples from 20 to 3672 ppm. The most V-enriched magnetite is from feldspar-rich host rocks where V content varies from 398-3672 ppm, with a median value of 534 ppm. In other host-rock types, V content varies from 20 to a maximum of 260 ppm. The Mn content shows the largest variability and ranges from 178 to 19259 ppm. The highest Mn-enriched magnetite is from Grt-Px samples, where Mn content varies from 1680-19259 ppm, with a remarkably high median value of 12925 ppm. In other host rock types, the Mn content in magnetite varies between 178 and 8469 ppm.

The Co content ranges in samples from 1 to 141 ppm. Similar to Mn the Co is enriched in magnetite from Grt-Px host-rock samples where Co content varies from 1-141 ppm, with a median value of 63 ppm. In other host-rock types the Co content is less than 78 ppm. The Ga content ranges in samples from 1 to 330 ppm with the most Ga enriched magnetite in Pl samples where Ga content varies from 145-196 ppm. Both Co and Ga show systematically lower concentrations in magnetite that co-occur with sulfide phases, particularly in Grt-Px and Px-Amf host rock types.

Also, the Cr content shows a large variability from 1 to 7248 ppm. The most Cr-enriched magnetite is found in feldspar-rich host rocks where Cr content has a median value of 915 ppm. Al content varies between 245 to 13300 ppm with the median of 2625 ppm, and Mg concentrations are between 11 and 1513 ppm with the median of 527 ppm.

The Ni content ranges in samples from 0.4 to 218 ppm, with also the highest values in feldspar-rich host rocks where Ni content varies from 87-218 ppm, with a median value of 141 ppm. In other host-rock types, the Ni content in magnetite is less than 48 ppm. The Ti content in magnetite ranges from 116 to 10 309 ppm. The most Ti-enriched magnetite is in plagioclase-rich host-rock samples where Ti content varies from 1759-9257 ppm, with a median value of 3299 ppm.

The Cu content is very low and ranges in samples from 0.02 to 5 ppm. The most Cu-enriched

magnetite is from Grt2 samples where Cu content varies from 0.3-5 ppm, with the median value of 4 ppm. The Zn content shows a large variability of 4 to 1835 ppm across all sample types. Content of Mo, Ag, and Sn is typically low (<50 ppm) but Sn content reaches 175 ppm in magnetite from Pl host-rocks. In Grt-Px and Px-Amp group samples with sulphides present, the magnetites were seemingly depleted by Co and Ga, having nearly ten times lower concentrations compared to the samples with no sulphides.

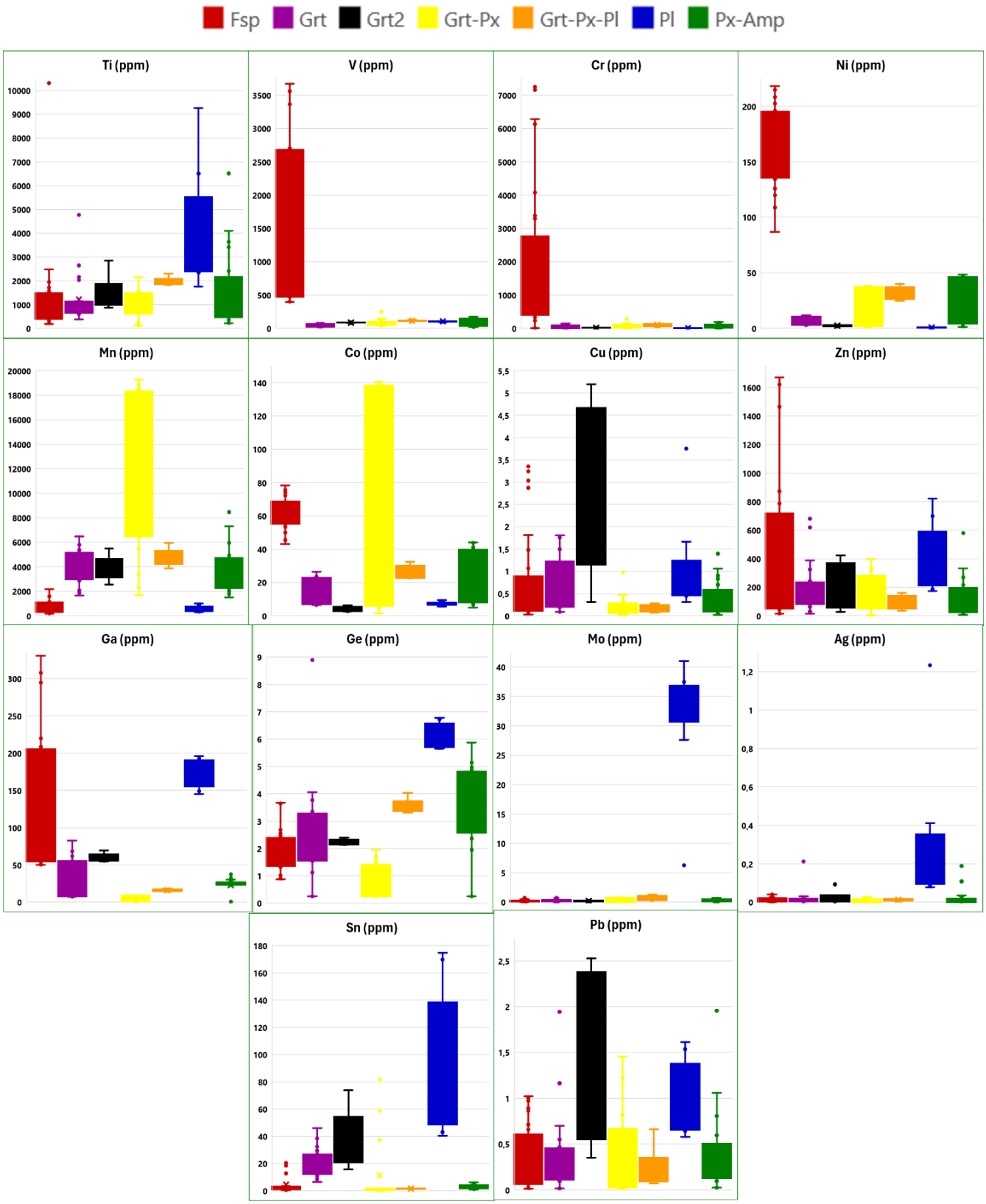

Figure 9. Trace elements variation in JMA magnetite in different host rock types: Feldspar (Fsp), Garnet (Grt), Garnet2 (Grt2), Garnet-Pyroxene (Grt-Px), Garnet-Pyroxene-Plagioclase (Grt-Py-Pl), Plagioclase (Pl), Pyroxene-Amphibole (Px-Amp).

Discussion

The origin of the JMA has puzzled researchers since its very first studies that have put forward several theories regarding the genesis of ore in the JMA. Linari (1940) suggests a skarn-like origin, whereas Vaganova and Kadyrova (1948) propose a metasomatic genesis. Tikhomirov (1966) characterizes these rocks as alternating layers of skarn, cummingtonite, biotite-sillimanite, and other hornfels, intersected by granite veins. However, the prevailing view is the concept of JMA formed during regional metamorphism of volcanogenic-sedimentary origin rocks, likely through the recrystallization and alteration of pre-existing iron-bearing minerals (Puura & Kuuspalu 1966; Erisalu et al. 1969). Also, Soesoo et al. (2020) remained inconclusive with regard to the JMA origin but noted that there are geological parallels between the Jõhvi area and the Bergslagen area in Sweden.

Dupuis & Beaudoin (2011) showed that the trace elements that can replace Fe in the magnetite crystal structure could be categorized into different groups based on their chemical properties and behaviour within the crystal structure of the mineral. Some common elements that can substitute for iron in magnetite include:

a) Transition Metal elements - Mn, Zn, Co, Cr, Ni, and Ti that can replace Fe in magnetite through solid solution substitutions and form various solid solution series with magnetite.
b) Mg that can also substitute for iron in magnetite, leading to the formation of magnesioferrite and other solid solution series within the mineral.
c) Al that can replace iron in magnetite, forming aluminomagnetite, which represents a solid solution series between magnetite and aluminomagnetite.
d) Other trace elements such as V and Ga that may also substitute for iron in magnetite, contributing to the overall chemical composition of the mineral.

All these substitutions allow discrimination of iron oxides between different mineral deposit types (Dupuis & Beaudoin 2011).

It is evident that JMA magnetite trace-element compositions plot on Ni+Cr vs. Si+Mg, and Al/(Zn+Ca) vs. Cu/(Si+Ca) diagrams outside the fields defined by Dupuis & Beaudoin (2011) for iron ores associated with Ni-Cu-PGE, and Cu-Zn-Pb VMS deposits, respectively (Figures 10, 11). There are some exceptions for some samples from the Fsp type, which plot in the Ni-Cu field on the Ni+Cr vs. Si+Mg diagram. Also, in Ti+V vs Ni/(Cr+Mn) diagram (Figure 12)

most of the JMA samples plot outside the fields for genetic types described in Dupuis & Beaudoin (2011) and also show lower Ni/(Cr+Mn) values than typical skarn deposits, except few exceptions from Fsp type samples which plot at the borders of IOCG, Porphyry or Fe-Ti, V fields.

Similarly, in Ti+V vs Ca+Al+Mn diagram (Figure 13) most of the JMA samples plot outside the fields for genetic types described in Dupuis & Beaudoin (2011) and also show lower Ti+V values than typical skarn deposits, except exceptions from Fsp and Pl type samples in which most of them plot in Porphyry field, and some of the Fsp type also in IOCG field. Also, all of the Soesoo et al. (2021) measured data plot at the uppermost part of the Porphyry field.

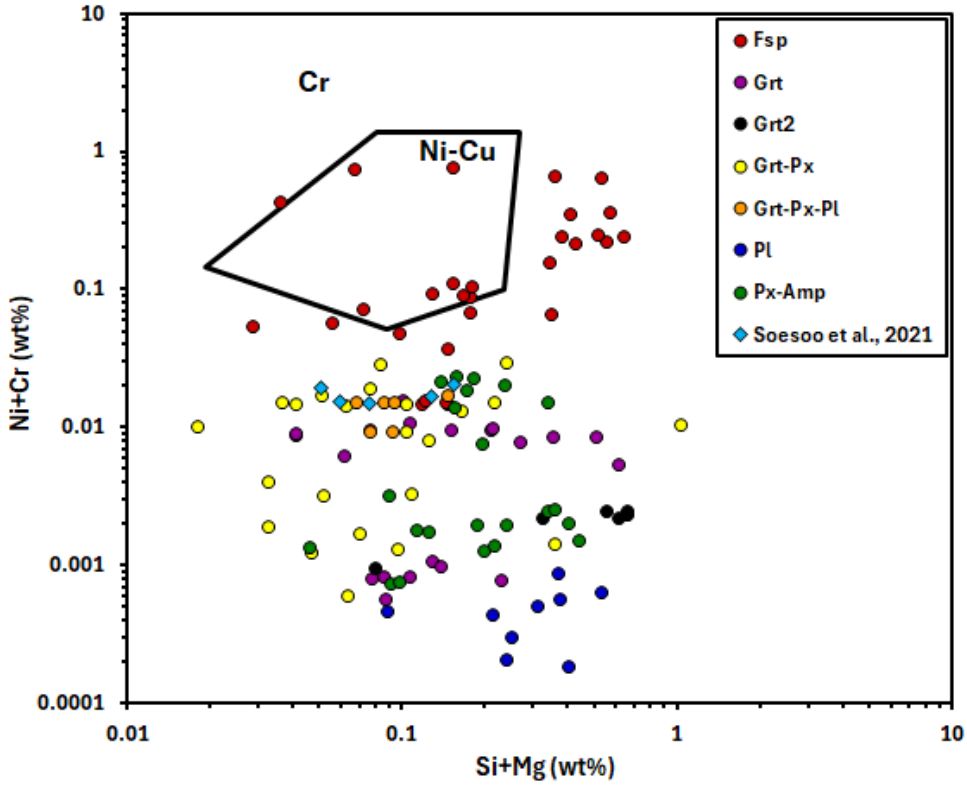

Figure 10. Magnetite chemical composition on the discriminant diagram Ni+Cr vs. Si+Mg after Dupuis & Beaudoin (2011). Also, JMA magnetite data from Soesoo et al. (2021) are shown.

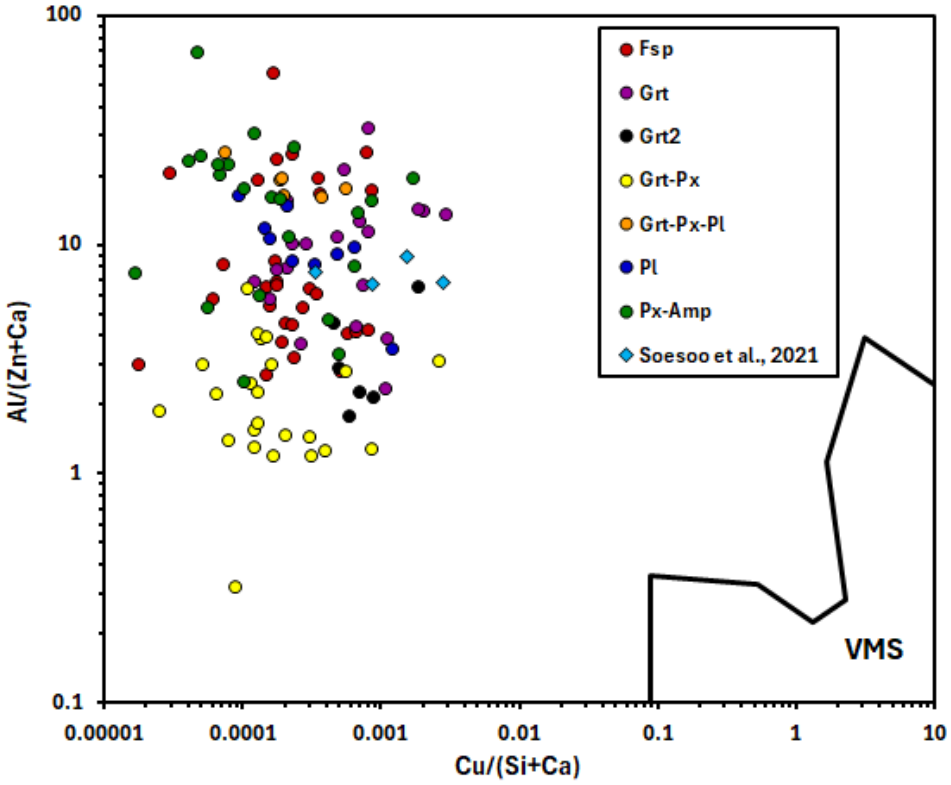

Figure 11. Magnetite chemical composition on the discriminant diagram Al/(Zn+Ca) vs. Cu/(Si+Ca) after Dupuis & Beaudoin (2011).

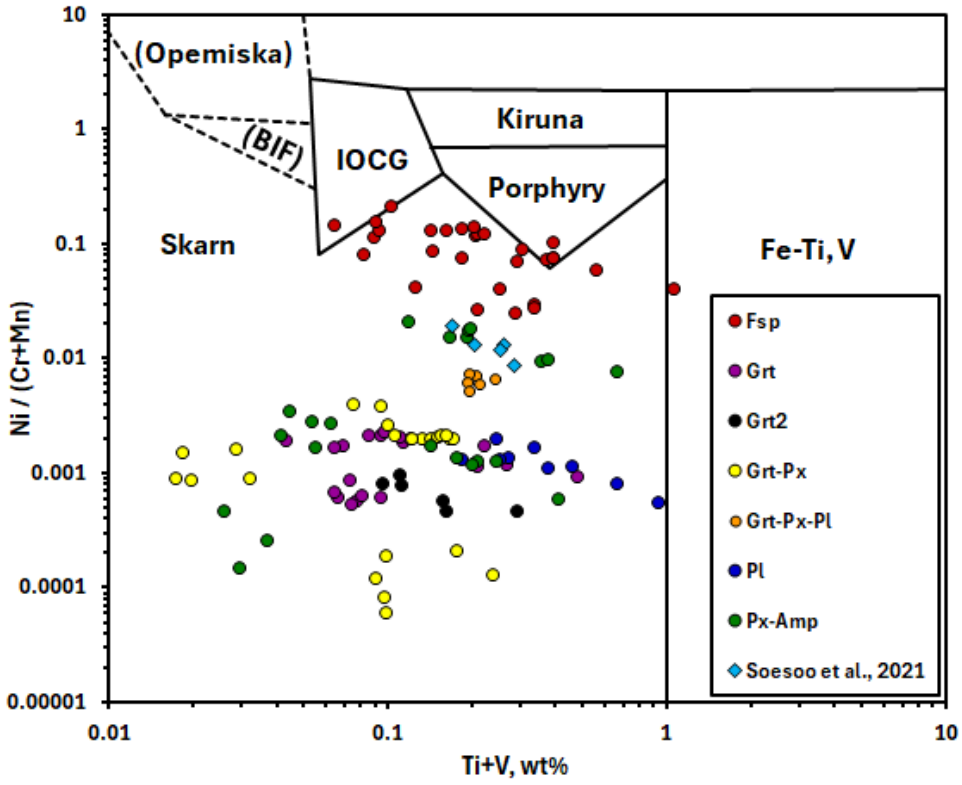

Figure 12. Magnetite chemical composition on the discriminant diagram: Ti + V vs Ni/(Cr + Mn) after Dupuis & Beaudoin (2011).

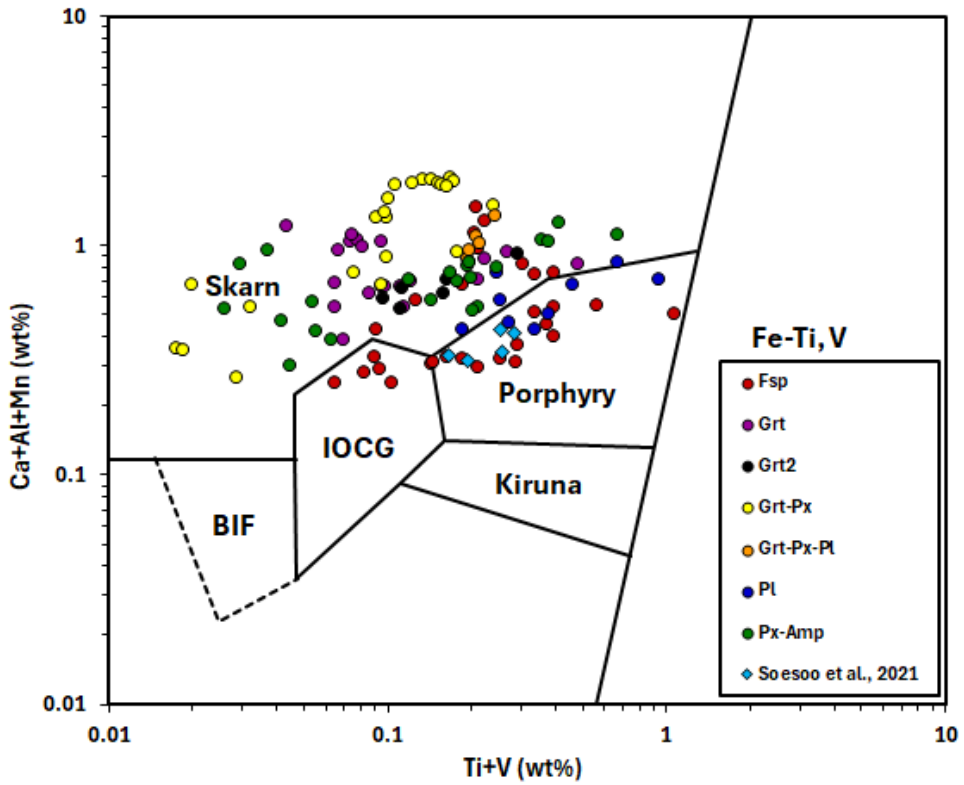

Figure 13. Magnetite chemical composition on discriminant diagram: Ti + V vs Ca+Al+Mn after Dupuis & Beaudoin (2011).

From the discriminant diagrams of Dupuis & Beaudoin (2011) it is evident that the trace-element composition of the JMA magnetites does not point to a single specific genetic type of the Fe-mineralization suggesting either different origin of the magnetite mineralization or overprinting of the magnetite trace-element signatures by secondary processes.

Nevertheless, Dupuis & Beaudoin (2011) also mention that hydrothermal iron-oxide ores of hydrothermal origin from different deposits do not plot into well-defined areas and are scattered all over the compositional field which might indicate that even if the JMA magnetite would have been specific ore type origin then later hydrothermal processes may have overprinted the original trace-element composition.

Interestingly, a secondary overprint on JMA magnetites is supported by the trace-element data showing large variations of several major trace-elements, particularly Mn, V, Cr, Mo, Ti and Ni that distinguish magnetites in JMA into several distinctive trace-element compositional groups that roughly match with the magnetite host rock types. This is further exemplified by the principal component analysis (PCA) of the magnetite trace elements (Figure 14) that shows

distinctively separate fields for magnetite in feldspar-bearing host rocks, plagioclase-rich host rocks and garnet–pyroxene host rocks. Magnetite in Fsp samples has a higher content of Ni, Cr and V, and also there is a group with elevated Co content Fsp type. Pl samples are characterized by a distinct Ag, Sn and Mo association, whereas Grt-Px type distinguishes with covariation to elevated Mn content.

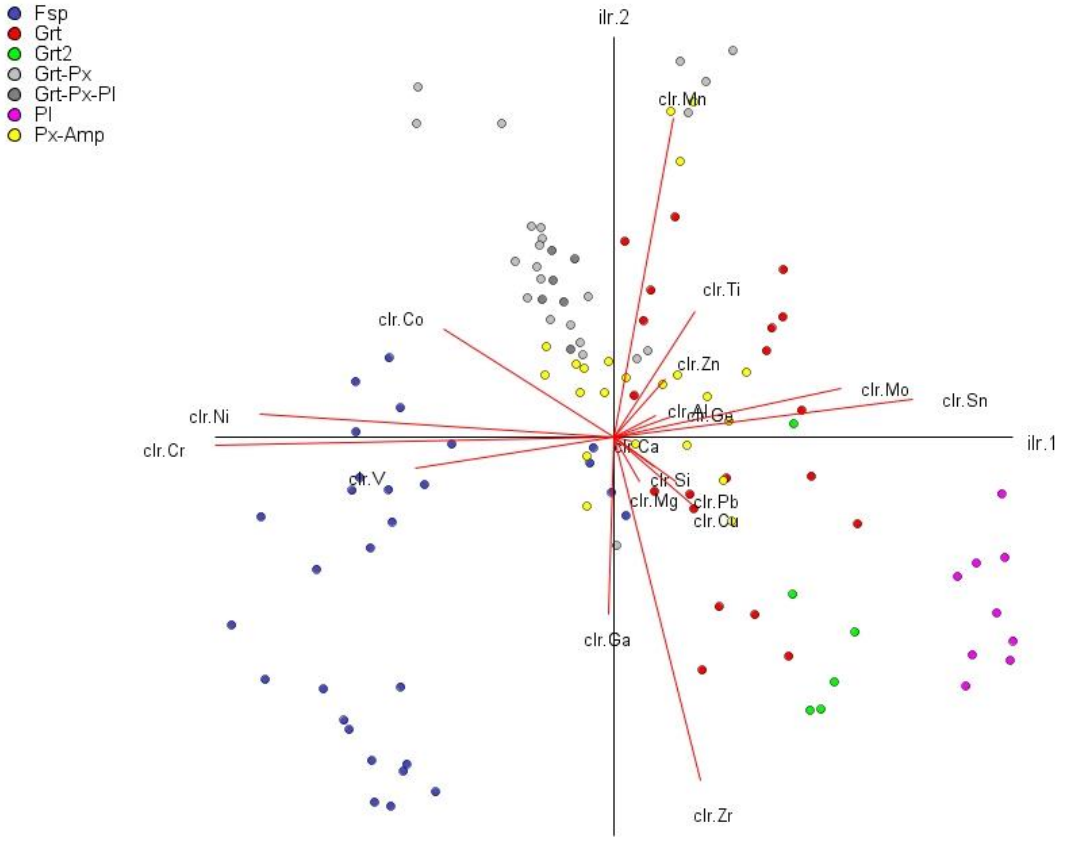

Figure 14. Plot of the PCA first and second principal components of log-ratio transformed JMA magnetite trace element concentrations. Note a clear separation of magnetites in feldspar-rich (Fsp) and in plagioclase-rich (Pl) host rock.

Magnetites in Pl host-rock have a higher content of Ag, Sn and Mo, which can be related to specific hydrothermal processes affecting the interval of the Pl-group. As hydrothermal fluids cool and react with surrounding rocks, metals like Ag and Sn can precipitate from the fluids and be incorporated into minerals like magnetite. Changes in temperature, pressure, and fluid composition (e.g., pH, redox conditions) can trigger the precipitation of these metals (Heinrich, 2007).

Grt-Px group distinguishes with higher Mn which is most likely from garnet species mineral spessartine. Grt-Px gneisses characterize typical granulite facies metamorphic rock (Soesoo et al., 2021). Even though there is variety in Grt-Px samples, they're most likely unaltered by hydrothermal fluids and major partial melting events.

Nevertheless, a large compositional variability of the magnetite in JMA clearly points to magnetite alteration in secondary processes. However, Nadoll et al. (2014) have suggested that it is difficult to attribute trace-element enrichments or depletions in magnetite to some simple process. They noted, for example, that hydrothermal skarn magnetite is characterized by elevated Mg, Al, Mn, Co, Ni, and Zn but it could have been caused by (a) elevated temperatures, (2) high concentrations of these elements in the hydrothermal fluids, or (3) intensive fluid–host rock interaction. Nadoll et al. (2014) also highlights that rock buffering is the most significant factor in controlling the composition of hydrothermal magnetite.

They propose overall relative discrimination criteria for the magnetite formed in different hydrothermal settings:

(I) BIF (hydrothermal) — low Al, Ti, V, Cr, Mn, Co, Ni, Zn, Ga and Sn;
(II) Ag–Pb–Zn veins (hydrothermal) — high Mn and low Ga and Sn;
(III) Mg-skarn (hydrothermal) — high Mg and Mn and low Al, Ti, Cr, Co, Ni and Ga;
(IV) skarn (hydrothermal) — high Mg, Al, Cr, Mn, Co, Ni and Zn and low Sn;
(V) porphyry (hydrothermal) — high Ti and V and low Sn;
(VI) porphyry (igneous) — high Ti, V and Cr and low Mg;
(VII) Climax-Mo (igneous) — high Al, Ga and Sn and low Mg and Cr;

Based on these trace-element enrichment-depletion criteria JMA magnetite and its host-rock types could be consolidated into 4 groups: feldspar, garnet, pyroxene and plagioclase groups (Figure 15). Magnetite in feldspar-rich host rock samples could be classified according to Nadoll et al. (2014) to the hydrothermal/igneous porphyry or hydrothermal skarn setting. Magnetite in garnet-rich host rock samples (includes Grt, Grt2 and Grt-Px types), and in pyroxene group samples (includes Grt-Px-Pl and Px-Amp types) are the most similar for hydrothermal Ag–Pb–Zn or BIF setting. Magnetite in Plagioclase group host-rock (Pl type) could also be classified as hydrothermal Ag–Pb–Zn setting. In figure 16 it is evident that garnet, pyroxene and plagioclase group magnetite trace-element diagrams look rather similar, and the only type which really stands out from others is feldspar group which corresponds according to

Nadoll et al. (2014) to the Porphyry hydrothermal and igneous settings.

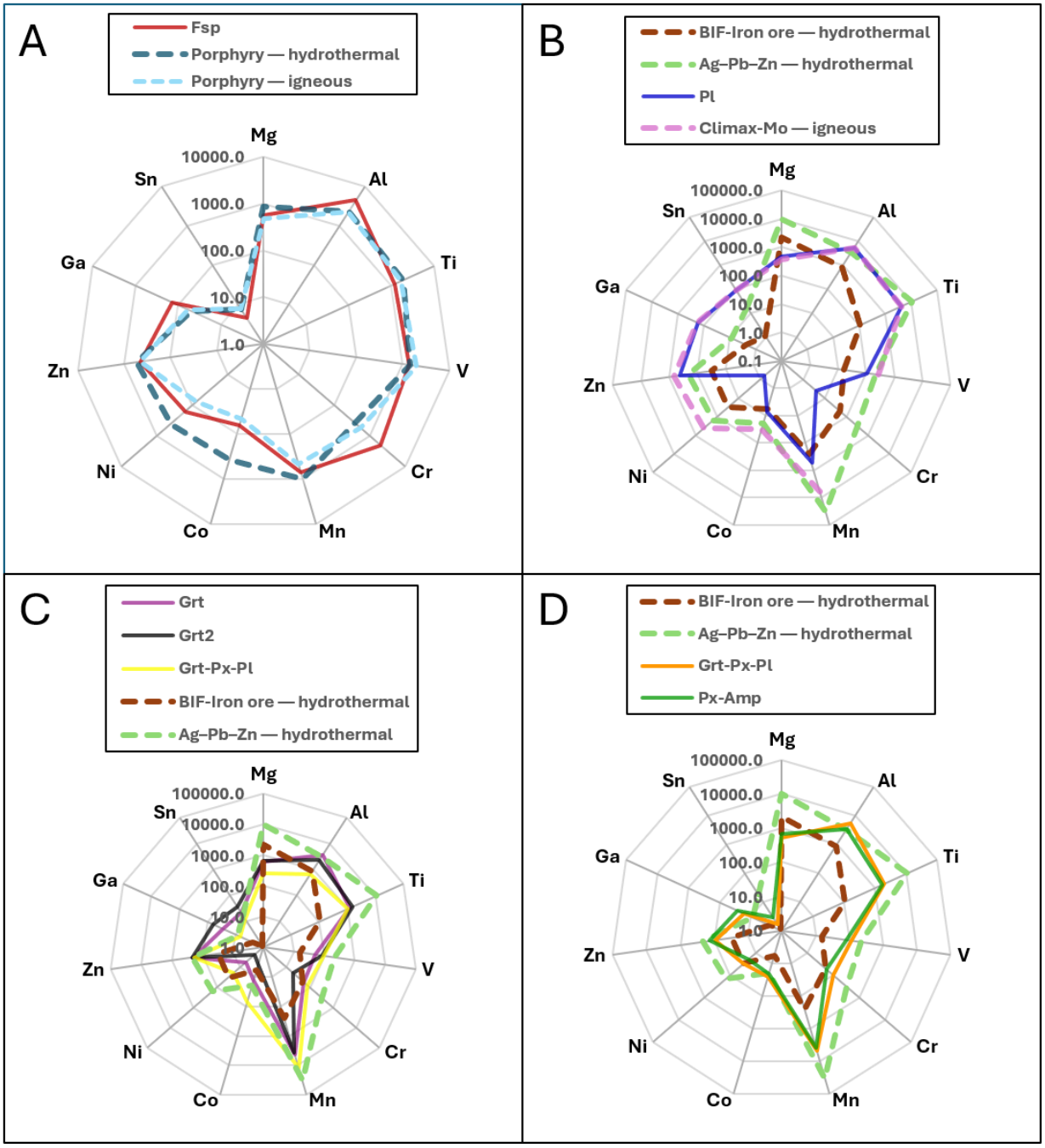

Figure 15. Magnetite chemical composition on discriminants diagram after Nadoll et al. (2014). A – Feldspar (Fsp) type compared to hydrothermal and igneous porphyry setting. B - Plagioclase (Pl) type compared to hydrothermal BIF and Ag–Pb–Zn vein settings, and igneous Climax-Mo setting. C - Garnet (Grt), Garnet2 (Grt2), Garnet-Pyroxene-Plagioclase (Grt-Py-Pl) types compared to hydrothermal BIF and Ag–Pb–Zn veins setting. D - Garnet-Pyroxene (Grt-Px) and Pyroxene-Amphibole (Px-Amp) types compared to hydrothermal BIF and Ag–Pb–Zn veins setting.

In addition, an important difference between magmatic and hydrothermal magnetite is the behavior of Ni and Cr. In silicate magmas, their behavior is coupled, with Ni/Cr ratios ≤1, as both behave compatibly during fractionation of intermediate and felsic melts However, in many hydrothermal settings, their behavior is decoupled and the Ni/Cr ratio of magnetite is typically higher (≥1), probably due to a higher solubility of Ni compared to Cr in fluids. This difference in behavior of Ni/Cr in fact appears to be the only way to distinguish magnetite from high-temperature hydrothermal deposits and felsic host rocks (such as I-type granite), which otherwise have very similar trace element signatures. Thus, a plot of Ti versus Ni/Cr can be used to discriminate magnetite between hydrothermal and all magmatic environments. (Dare et al., 2014)

Discriminant diagram Ti vs Ni/Cr (Figure 17) of Dare et al. (2014) shows that the majority of the magnetite samples plot on magmatic field, which could be related to granulitic metamorphism of rocks in JMA that has most likely overprinted the initial magnetite trace element composition. However, some magnetite samples plot in the hydrothermal field, which probably indicates that they were altered by hydrothermal fluids even after the major metamorphism process.

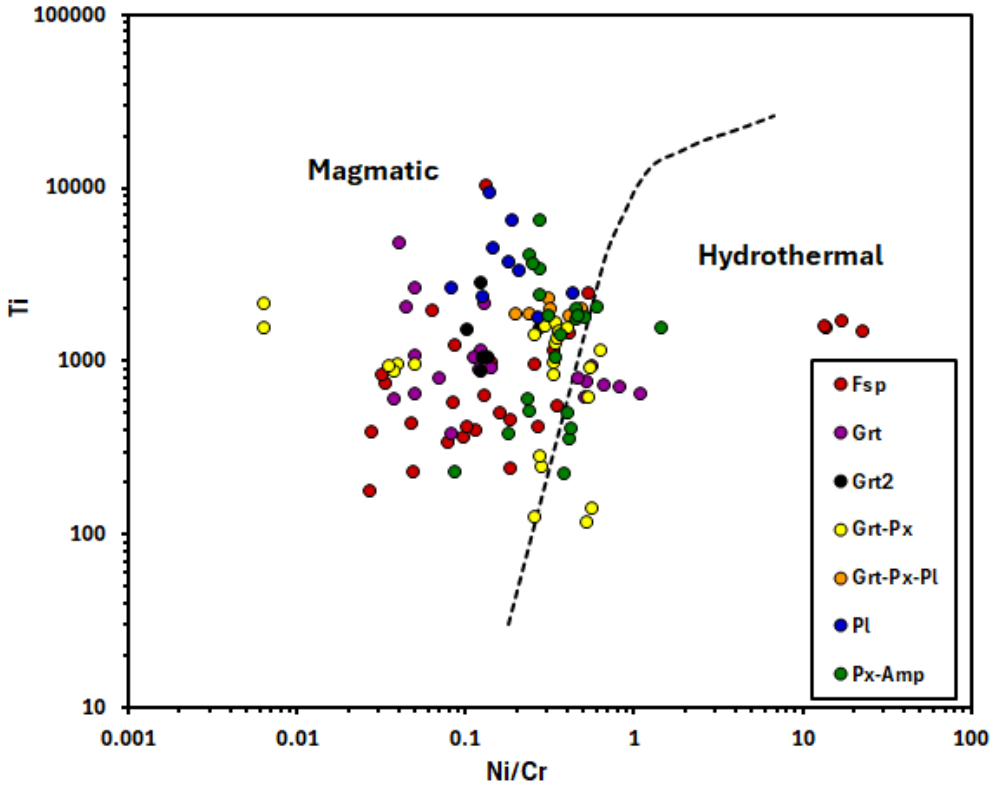

Figure 17. Magnetite chemical composition on discriminant diagram Ti vs. Ni/Cr after Dare et al. (2014).

Conclusions

- JMA magnetite trace-element composition depends on the host-rock mineral composition.
- The discriminant diagrams of Dupuis & Beaudoin (2011) indicate that the trace-element composition of JMA magnetites does not correspond to a single genetic type of Fe-mineralization, suggesting either a diverse origin or overprinting by secondary processes e.g. metamorphism, partial melting or hydrothermal alteration.
- Also, PCA reveals the significant variation in major trace elements, notably Mn, V, Cr, Mo, Ti, and Ni, among JMA magnetites indicating a secondary overprint, delineating distinct trace-element compositional groups corresponding to magnetite host rock types.
- Magnetite multi-element chemical composition discriminant diagrams of Nadoll et al. (2014) suggest that the majority of the JMA magnetite correspond to Ag–Pb–Zn or BIF setting with exception of magnetite in feldspar host-rock that corresponds to hydrothermal or igneous Porphyry settings.
- The discriminant diagram Ti vs Ni/Cr by Dare et al. (2014) indicates that the majority of JMA magnetite have magmatic origin, which has been altered by granulitic metamorphism, and also some cases by hydrothermal fluids.
- Given that the Gr-Px group magnetite is the least altered by secondary processes it could be suggested that likely JMA magnetite had BIF type iron-ore origin but has been severely altered in later hydrothermal processes overprinting the original trace-element composition.
- The study of the origin of the initial mineralization in the Jõhvi magnetite-rich gneisses using various methods revealed that in complex metamorphic systems, where multiple factors can alter the trace-element composition in magnetites, determining a definitive answer is challenging.
- Therefore, in similar settings, it is crucial to have a representative set of samples to account for all possible processes that could have affected the formation and altered the trace element composition in magnetite grains.

Composition of magnetite trace elements in the Jõhvi magnetic quartzite in north-east Estonia as an indicator of iron mineralisation processes

Alvar Ratt

Summary

This thesis investigated Jõhvi magnetic anomaly cores PA-1 and PA-2 intervals where magnetite occurs. The aim of the thesis was to determine the origin of the iron-ore in JMA using the magnetite trace-element content characteristic. Altogether, 17 samples from intervals of magnetite mineralisation were sampled and analysed of which 10 samples were thin-sections and 7 thick-sections. The petrography of the samples was described, and the trace element composition was measured. The mineralogy of the samples was analysed by scanning electron microscopy (SEM) and the presence of trace elements by laser ablation inductively coupled plasma mass spectrometry (LA-ICP-MS). The main trace elements used were V, Cr, Ni, Ti and Mn which were analysed in 115 different magnetite grains.

Magnetite in Jõhvi magnetic anomaly rocks is found in several intensively mineralised zones throughout the Jõhvi crystalline rock succession that frequently co-occurs with sulfide mineralisation. The magnetite typically forms xenoblastic grains that mainly occur as 1-3 mm directional and elongated grains, but there are also massive aggregates or separate and rounded xenoblastic grains.

Trace-element composition discriminant diagrams show that magnetite composition in JMA plots outside of the typical iron deposits fields and most likely the trace-element composition of the JMA magnetite has been significantly altered by later hydrothermal processes overprinting the original trace-element composition. This is evidenced by large variations in trace-element compositions whereas the principal component analysis of the magnetite trace-element compositions shows three distinctive groups in JMA magnetites: (a) magnetite in feldspar-bearing host rock, (b) magnetite in plagioclase-rich host rocks and (b) magnetite in garnet–pyroxene host rock. Magnetites in Fsp host-rock have a higher content of Ni, Cr and V, and also there is a group with elevated Co content in Fsp type. Grt-Px type samples are characterized by covariation to elevated Mn content, whereas Pl samples distinguishes with a distinct Ag, Sn and Mo association. The Gr-Px group magnetite is the least altered by secondary processes, and it could be suggested that the JMA magnetite had BIF-type iron-ore

origin, but the iron-ore has been severely altered in later hydrothermal processes overprinting the original trace-element composition. It must be concluded that magnetite trace element analysis and discrimination is not a straightforward method for revealing the strongly altered JMA iron-ore deposit origin.

Kokkuvõte

Käesolevas töös uuriti 2019. aastal Jõhvi läänepoolseimasse magnetanomaaliasse puuritud puursüdamikes PA-1 ja PA-2 intervalle, kus esineb magnetiiti. Selleks kirjeldati ja analüüsiti 17 proovi, millest 10 õhikud ja 7 lihvid. Kirjeldati proovide petrograafiat ja määrati neis esinevaid jälgelemente, mille põhjal iseloomustati nende tekketingimusi. Proovide mineraloogilist koostist analüüsiti skaneeriva elektronmikroskoobiga (SEM) ja jälgelementide esinemist laser-ablatsiooni induktiivsidestatud plasma massi-spektromeeriga (LA-ICP-MS). Jälgelementidest määrati magnetiitides V, Cr, Ni, Ti and Mn sisaldusi kokku 115 erinevast magnetiidi terast.

Magnetiit esineb Jõhvi magnetilise anomaalia kivimites mitmete intensiivselt mineraliseerunud tsoonidena, mis sageli esinevad koos sulfiidide mineralisatsiooniga. Magnetiit moodustab tavaliselt ksenoblastilisi teralisi masse, milles magnetiidi terad esinevad peamiselt 1-3 mm suuruste suunatud - välja venitatud teradena, kuid esineb ka massiivseid kogumikke või eraldi ja ümaramaid ksenoblastilisi terasid.

Magnetiidi jälgelementide koostise diskriminant-diagrammid näitavad, et magnetiit jääb väljapoole tüüpilisi raua geneesi väljadest ja tõenäoliselt JMA magnetiitide jälgelementide signaal tugevalt mõjutatud hiljematest hüdrotermaalseste protsessidest. Magnetiidi mikroelementide koostise põhikomponentanalüüs näitas kolme rühma eristumist: (a) magnetiit päevakivide, (b) plagioklassirikas ja (c) granaat-pürokseeni koostisega ümbriskivimis. Päevakivi tüüpi ümbriskivimiga proovide magnetiit eristub kõrgemate Ni, Cr ja V sisaldustega, samuti mõningatel juhtudel ka kõrgema Co sisaldusega. Granaat-pürokseen ümbriskivimis on magnetiidile iseloomulik kovariatsioon kõrgema Mn-sisaldusega, samas kui plagoklassi tüüpi ümbriskivimis eristuvad selgelt kõrgemate Ag, Sn ja Mo sisaldustega magnetiidid.

Gr-Px rühma magnetiiti on sekundaarsete protsesside abil kõige vähem muutunud ja snende manetiitide jälgelementide suhete alusel võiks oletada, et JMA magnetiidil oli BIF-tüüpi rauamaagi päritolu, kuid maak on hilisemates hüdrotermaalsetes protsessides tugevalt muutunud.. Kokkuvõtteks tuleb järeldada, et magnetiidi jälgelementide analüüs ja klassifitseerimine ei ole otseselt ning ühemõtteliselt kasutatav tugevalt sekundaarsetes protessides muutunud rauamaakide nagu JMA algse päritolu selgitamiseks.

Acknowledgments

The author would like to express the gratitude to supervisors Kalle Kirsimäe and Siim Nirgi for helping with every aspect. Also, Peeter Paaver for his assistance in the use of inductively coupled plasma mass spectrometry (ICP-MS).

References

Aitchison, J., Barceló-Vidal, C., Martín-Fernández, J. A., & Pawlowsky-Glahn, V. (2000). Logratio analysis and compositional distance. *Mathematical geology*, *32*, 271-275.

Dupuis, C., & Beaudoin, G. (2011). Discriminant diagrams for iron oxide trace element fingerprinting of mineral deposit types. *Mineralium Deposita*, *46*, 319-335. doi:10.1007/s00126-011-0334-y

Erisalu, E., Arvisto, E., Norman, A., Dantsenko, V., Koppelmaa, H., Niin, M., & Kivisilla, J. (1969). Otchet po izucheniyu kristallicheskogo fundamenta Jyhviskoj magnitnoj anomalii i ee okrestnostej [Report of the Basement Studies on Jõhvi Magnetic Anomaly and Nearby]. *Geological Survey of Estonia, Tallinn, EGF*, *3032*, 257. [In Russian]

Heinrich, C. A. (2007). Fluid-fluid interactions in magmatic-hydrothermal ore formation. *Reviews in Mineralogy and Geochemistry*, *65*(1), 363-387. doi:10.2138/rmg.2007.65.11

Jafari, A., Karimpour, M. H., Mazaheri, S. A., Shafaroudi, A. M., & Ren, M. (2019). Geochemistry of metamorphic rocks and mineralization in the Golgohar iron ore deposit (No. 1), Sirjan, SE Iran: Implications for paleotectonic setting and ore genesis. *Journal of Geochemical Exploration*, *205*, 106330. doi:10.1016/j.gexplo.2019.06.012

Kirs, J., Puura, V., Soesoo, A., Klein, V., Konsa, M., Koppelmaa, H., ... & Urtson, K. (2009). The crystalline basement of Estonia: rock complexes of the Palaeoproterozoic Orosirian and Statherian and Mesoproterozoic Calymmian periods, and regional correlations. *Estonian Journal of Earth Sciences*, *58*(4). doi:10.3176/earth.2009.4.01

Koppelmaa, H., Kivisilla, J., Klein, V., All, T. (2002). Geological Map of the Crystalline Basement of Estonia. Scale 1:400 000. Explanation to the Map. Geological Survey of Estonia, Tallinn.

Leach, D. L., Bradley, D. C., Huston, D., Pisarevsky, S. A., Taylor, R. D., & Gardoll, S. J. (2010). Sediment-hosted lead-zinc deposits in Earth history. *Economic Geology*, *105*(3), 593-625. doi:10.2113/gsecongeo.105.3.593

Linari, A. A. (1940). Aruanne sügavpuurimistest Jõhvi lähedal [Report on diamond drilling near Jõhvi]. *Tallinna Tehnikaülikooli Toimetused*, 1-27. [In Estonian]

Luha, A., 1946. Earth Resources in the USSR. Concluding Overview of Geological Appliances. *Teaduslik Kirjandus*, Tartu, pp.1–176. [In Estonian]

Klein, C. (2005). Some Precambrian banded iron-formations (BIFs) from around the world: Their age, geologic setting, mineralogy, metamorphism, geochemistry, and origins. *American Mineralogist*, *90*(10), 1473-1499. doi:10.2138/am.2005.1871

Mao, J., Bierlein, F. P., Beaudoin, G., Hébert, R., Wang, C. S., & Tang, J. (2005). Epithermal Au-Ag-Cu, porphyry Cu-(Au-Mo) and Cu-Au-Ag-Zn-Pb skarn deposits of the Gangdese Arc, Tibet. In *Mineral Deposit Research: Meeting the Global Challenge: Proceedings of the Eighth Biennial SGA Meeting Beijing, China, 18–21 August 2005* (pp. 1219-1222). Springer Berlin Heidelberg. doi:10.1007/3-540-27946-6_311

Nadoll, P., Angerer, T., Mauk, J. L., French, D., & Walshe, J. (2014). The chemistry of hydrothermal magnetite: A review. *Ore geology reviews*, *61*, 1-32. doi:10.1016/j.oregeorev.2013.12.013

Nirgi, S., Maala, L., Kaasik, T., Smyth, D., Wrobel, F. (2022). Assessment of the Exploration Potential of the Jõhvi Magnetic Anomaly, NE Estonia.

Nirgi, S., Soesoo (2021). A. Geology and geochemistry of a paleoproterozoic iron mineralization in North-Eastern Estonia. Transactions of the Karelian Research Centre of the Russian Academy of Sciences, (10), 25-43. doi:10.17076/geo1492

Plado, J., Kiik, K., Jokinen, J., & Soesoo, A. (2020). Magnetic anomaly of the Jõhvi iron ore, northeastern Estonia, controlled by subvertical remanent magnetization. *Estonian Journal of Earth Sciences*, *69*(4), 189-199. doi:10.3176/earth.2020.13

Puura, V., & Kuuspalu, T. (1966). Metallogenicheskaya karta Éstonskoj SSR m-ba 1: 500 000. Otchet III. Rudoproyavleniya v kristallicheskom fundamente uchastkov Yyhvi i Ulyaste [Map of Metallogeny of the Estonian SSR in a Scale of 1: 500 000. Volume III. Ore Occurrences in the

Crystalline Basement of Jõhvi and Uljaste Areas]. *Geological Survey of Estonia, Tallinn, EGF, 2801*, 267.

Puura, V., & Flodén, T. (1996). Subjotnian igneous structures in the Svecofennian domain of the Baltic region. *GFF, 118*(S4), 22-23. doi:10.1080/11035899609546289

Ratt, A., 2022. Pyrrhotite and pyrite trace element composition in Jõhvi magnetite quartzites, north-east Estonia: implications to sulphide mineralisation processe. University of Tartu. Geology department. Bachelor's thesis. 1-45.

Robb, L. (2020). Introduction to ore-forming processes. *John Wiley & Sons*.

Skirrow, R. G. (2022). Iron oxide copper-gold (IOCG) deposits–A review (part 1): Settings, mineralogy, ore geochemistry and classification. *Ore Geology Reviews, 140*, 104569. doi:10.1016/j.oregeorev.2021.104569

Soesoo, A. (2004). Precambrian basement of Estonia. *Proceedings of the Estonian Academy of Sciences, Geology, Special Issue, 53*, 147-148.

Soesoo, A., Nirgi, S., Plado, J. (2020). The evolution of the Estonian Precambrian basement: geological, geophysical and geochronological constraints. Proceedings of the Karelian Research Centre of the Russian Academy of Sciences, 10, 18–33.

Soesoo, A., Nirgi, S., Urtson, K., & Voolma, M. (2021). Geochemistry, mineral chemistry and pressure-temperature conditions of the Jõhvi magnetite quartzites and magnetite-rich gneisses, NE Estonia. *Estonian Journal of Earth Sciences, 70*(2). doi:10.3176/earth.2021.05

Suuroja, K., 1969. Jõhvi magnetiitse maagistumise iseloomust. Tartu Ülikool, Geoloogia kateeder. Diplomitöö.1–88.

Tikhomirov, S. N. (1966). Geologicheskoe stroenie dokembrijskogo fundamenta v predelakh Leningradskoj oblasti i Pribaltiki [Geology of the Crystalline Basement in Leningrad Oblast and Baltics]. *VSEGEI, Leningrad*. 24. [in Russian].

Vaganova, Z. & Kadyrova, M. 1948. Dokembrijskie kristallicheskie porody i zhelezistye kvartsity Ést. SSR [Precambrian Crystalline Rocks and Iron-Rich Quartzites of the Estonian S.S.R.]. Ministry of Geology of the S.S.S.R., Leningrad. 228. [in Russian]

Vaher, R., Puura, V., Erisalu, E., 1962. The tectonic pattern of Northeast Estonia. ENSV TA Geoloogia Instituudi Uurimused, 319–335. [In Russian]

Yıldırım, N., Dönmez, C., Kang, J., Lee, I., Pirajno, F., Yıldırım, E., Günay, K., Seo, J.H., Farquhar, J. and Chang, S.W. (2016). A magnetite-rich Cyprus-type VMS deposit in Ortaklar: A unique VMS style in the Tethyan metallogenic belt, Gaziantep, Turkey. *Ore Geology Reviews*, *79*, 425-442. doi:10.1016/j.oregeorev.2016.05.021

Appendices

Appendix 1. LA-ICPMS analysis results of magnetite grains

Sample ID	Mg (ppm)	Al (ppm)	Si (ppm)	Ca (ppm)	Ti (ppm)	V (ppm)	Cr (ppm)	Mn (ppm)	Co (ppm)	Ni (ppm)	Cu (ppm)	Zn (ppm)	Ga (ppm)	Ge (ppm)	Mo (ppm)	Ag (ppm)	Sn (ppm)	Pb (ppm)
TS-00025-2-1	752.61	5579.57	4624.01	797.27	736.31	2658.72	6131.82	1126.47	69.04	208.36	1.07	713.07	168.50	1.53	0.11	0.01	1.72	0.39
TS-00025-2-3	379.52	3554.41	3271.10	466.53	826.40	2535.43	6288.82	1140.96	53.43	203.48	0.23	151.30	144.26	1.40	0.12	0.04	1.36	0.66
TS-00025-4-3	528.89	5229.76	2951.12	438.26	635.67	1217.03	1354.97	1038.23	61.06	175.58	0.71	723.03	135.43	1.01	0.07	0.01	2.57	0.86
TS-00025-1-3	150.23	2106.25	528.83	73.80	177.34	2704.85	7160.33	910.22	54.51	196.03	0.22	52.89	131.31	1.32	0.07	0.00	0.31	0.40
TS-00025-4-4	728.34	4359.59	3382.80	755.03	229.45	1028.91	3289.16	719.91	59.55	162.64	0.63	873.11	115.61	0.87	0.04	0.00	1.43	1.00
TS-00025-3-2	140.71	2473.55	225.20	50.72	439.58	2083.50	4075.98	714.47	56.37	193.84	0.24	93.87	114.39	1.71	0.09	0.00	0.61	0.06
TS-00025-3-1	253.03	2182.30	1290.11	264.97	387.63	1730.84	7248.06	511.13	55.79	202.51	0.47	78.42	106.37	1.39	0.08	0.00	0.38	0.44
TS-00027-4A	761.77	4335.15	5017.38	767.66	1947.16	3672.07	3380.09	432.40	55.10	218.39	3.36	295.94	219.88	2.67	0.33	0.03	3.59	1.02
TS-00027-2-3	870.10	7148.43	5575.01	909.65	361.92	2706.55	2187.39	244.06	62.85	214.87	1.48	711.90	208.28	3.67	0.29	0.00	12.76	0.38
TS-00027-3-3	471.11	3729.19	3375.74	586.39	339.33	3365.50	2174.31	238.50	54.08	172.73	3.24	294.88	205.88	2.09	0.13	0.03	1.86	0.89
TS-00027-3-1	778.08	6608.38	4843.35	713.91	571.43	3394.62	2025.46	322.74	68.41	172.47	2.87	1670.72	203.83	2.01	0.37	0.04	1.44	0.97
TS-00027-2A	440.35	3204.50	3888.51	624.44	396.98	3559.83	1876.15	214.41	43.18	215.38	3.03	147.74	194.21	3.65	0.25	0.01	2.48	0.39
TS-00027-1A	412.88	4549.55	4778.42	526.20	1222.57	2701.23	2226.03	368.66	45.46	193.09	1.82	222.30	168.33	2.73	0.11	0.04	1.21	0.71
J_PA1-2-24A	1026.00	13300.00	445.00	217.50	1560.50	533.40	9.78	1155.50	78.40	136.20	0.10	1835.00	330.25	0.92	0.20	0.01	18.55	0.02
J_PA1-2-25A	761.00	8425.00	422.50	222.50	1570.00	529.15	9.81	1096.50	62.65	134.45	0.11	786.00	294.30	1.04	0.30	0.02	20.51	0.01
J_PA1-2-26A	992.00	11550.00	460.00	215.00	1710.00	534.00	8.19	1142.50	72.30	139.80	0.12	1465.00	297.10	0.97	0.24	0.01	20.75	0.11
J_PA1-2-27A	780.00	9975.00	450.00	232.50	1486.50	563.90	6.49	1082.50	62.65	148.90	0.11	1620.00	307.80	0.90	0.29	0.01	20.48	0.27
TS-00024-1-1	217.97	2253.77	70.26	32.03	552.63	488.32	387.95	254.53	74.17	136.17	0.08	58.20	59.38	1.82	0.11	0.02	1.43	0.04
TS-00024-2-1	715.48	2911.28	1063.58	33.96	494.49	402.45	736.80	319.28	67.86	119.81	0.03	109.95	57.91	2.70	0.72	0.00	2.94	0.55
TS-00024-5-1	302.47	2537.47	261.00	69.23	1154.58	474.52	415.76	641.87	75.66	138.64	0.12	62.94	57.90	2.24	0.03	0.01	2.15	0.05

Sample ID	Mg (ppm)	Al (ppm)	Si (ppm)	Ca (ppm)	Ti (ppm)	V (ppm)	Cr (ppm)	Mn (ppm)	Co (ppm)	Ni (ppm)	Cu (ppm)	Zn (ppm)	Ga (ppm)	Ge (ppm)	Mo (ppm)	Ag (ppm)	Sn (ppm)	Pb (ppm)
TS-00024-2-3	225.63	2057.38	499.06	285.31	240.38	404.17	589.88	177.64	50.04	108.88	0.14	28.29	56.40	2.46	0.01	0.01	1.01	0.03
TS-00024-4-1	297.92	2506.88	695.28	1.67	1443.86	419.58	330.68	702.48	72.25	136.33	0.12	43.60	55.12	1.74	0.21	0.02	1.82	0.05
TS-00024-1-3	532.03	2294.70	1144.66	246.66	457.45	486.72	759.94	335.06	68.77	141.20	0.33	473.65	54.45	1.78	0.16	0.02	1.40	0.42
TS-00024-4A	625.17	2464.32	1173.08	57.76	961.72	472.67	528.11	546.41	67.87	137.88	0.22	48.39	54.39	1.79	0.11	0.00	1.35	0.32
TS-00024-3-1	499.94	2170.26	802.56	377.18	415.27	411.93	840.40	263.98	59.50	86.95	0.33	32.50	53.89	2.18	0.05	0.00	1.36	0.38
TS-00024-2-4	604.04	2604.99	1199.11	246.42	10308.57	397.51	915.26	2187.26	68.10	121.84	0.11	72.77	53.59	2.55	0.45	0.01	3.15	0.13
TS-00024-4-4	527.05	2369.54	1027.05	80.26	975.62	472.26	949.52	638.03	66.73	135.19	0.26	16.16	53.06	1.76	0.07	0.00	1.14	0.16
TS-00024-3-2	515.96	2029.21	970.53	91.10	2475.57	435.53	234.71	1586.69	64.12	125.92	0.14	16.37	50.59	1.81	0.05	0.00	1.21	0.07
TS-00024-1-2	962.96	2949.01	2558.41	976.01	417.31	498.24	503.62	392.00	65.95	138.16	0.06	14.65	49.98	2.32	0.12	0.00	0.87	0.11
TS-00035-1-5	1345.58	9350.80	4861.81	689.22	378.29	57.32	49.42	2138.57	15.69	4.08	0.68	680.20	82.38	4.06	0.89	0.01	46.05	0.23
TS-00035-2-3	883.09	5348.57	4225.57	680.84	2644.26	55.46	78.99	3390.02	15.36	4.00	0.77	242.96	68.87	8.90	0.77	0.00	12.01	0.28
TS-00035-1-8	575.20	3913.58	2136.94	323.93	2027.56	74.42	74.25	2848.03	7.13	3.35	0.71	68.09	68.41	3.77	0.17	0.01	13.18	0.21
TS-00035-4A	409.55	2625.23	3172.90	682.36	1075.48	65.02	80.15	2087.64	6.83	4.02	1.01	29.62	61.85	3.37	0.12	0.00	11.04	0.39
TS-00035-4-1	220.31	2179.62	405.65	54.19	639.40	57.46	57.21	1665.56	6.36	2.89	0.38	14.39	55.19	2.55	0.06	0.02	8.62	0.25
35-48A	11.00	3340.00	405.65	180.00	596.00	54.50	83.20	1878.00	8.03	3.18	1.20	61.30	55.19	0.25	0.75	0.00	6.41	0.22
35-49A	11.00	4430.00	405.65	180.00	4765.00	63.75	85.00	3710.00	12.70	3.42	1.76	150.70	55.19	0.25	0.75	0.00	9.39	0.47
J_PA2-2-33A	888.00	5840.00	195.53	255.00	713.00	27.03	4.45	4360.00	12.50	3.69	0.32	213.00	11.02	1.59	0.16	0.02	29.50	0.10
J_PA2-2-34A	668.45	5428.00	195.53	217.50	751.50	26.71	5.40	4908.50	7.48	2.82	0.10	325.75	11.13	1.20	0.09	0.00	32.44	0.02
J_PA2-2-37A	591.50	5395.00	195.53	225.00	927.50	26.82	5.00	4711.50	6.92	2.81	0.09	122.00	11.98	1.12	0.08	0.02	25.15	0.02
J_PA2-2-38A	686.00	4620.00	195.53	205.00	640.00	25.12	2.64	4788.00	9.41	2.87	0.09	388.00	11.22	1.54	0.11	0.01	26.90	0.02
TS-00036-5-1	737.90	1996.42	1401.54	235.22	2153.53	66.83	83.66	6470.83	23.66	11.00	1.80	619.06	8.45	3.35	0.37	0.01	38.41	0.70
TS-00036-5-2	663.34	1527.16	1505.12	147.25	889.51	65.48	87.29	4928.82	23.55	10.57	1.12	202.17	8.41	3.04	0.22	0.21	25.86	1.16

Sample ID	Mg (ppm)	Al (ppm)	Si (ppm)	Ca (ppm)	Ti (ppm)	V (ppm)	Cr (ppm)	Mn (ppm)	Co (ppm)	Ni (ppm)	Cu (ppm)	Zn (ppm)	Ga (ppm)	Ge (ppm)	Mo (ppm)	Ag (ppm)	Sn (ppm)	Pb (ppm)
TS-00036-2-3	783.68	4991.48	1530.71	288.25	720.62	23.31	4.54	5798.22	6.59	3.03	1.50	153.82	8.41	2.63	0.34	0.01	23.18	0.55
TS-00036-5-3	615.32	1457.43	901.59	187.30	911.84	66.42	81.61	5048.94	23.65	11.65	1.23	187.61	8.35	2.83	0.30	0.03	24.33	0.42
TS-00036-1A	877.49	4395.14	430.38	67.11	795.45	22.84	7.17	5390.52	6.82	3.33	0.27	139.62	7.87	2.77	0.28	0.01	20.74	0.19
TS-00036-3A	579.17	1775.18	195.53	60.41	1139.86	65.71	82.55	5169.59	24.89	10.32	0.19	210.15	7.65	2.44	0.25	0.01	19.35	0.11
TS-00036-4-3	587.62	1465.39	435.77	53.39	797.14	65.70	141.58	4670.67	21.07	10.01	0.24	82.87	7.54	2.35	0.20	0.01	19.40	0.38
TS-00036-2-2	506.59	1900.05	889.77	53.13	618.47	24.87	6.38	4926.79	9.80	3.32	1.77	82.03	7.40	2.39	0.20	0.02	19.99	1.94
TS-00036-4-1	610.76	1466.16	463.47	32.74	1055.66	64.39	94.87	5166.90	26.52	10.68	0.09	156.71	7.35	2.92	0.27	0.01	20.00	0.11
TS-00010-2A	652.54	2787.26	158.81	5.43	1546.90	85.31	7.23	4328.11	6.13	1.99	0.31	423.91	69.13	2.40	0.15	0.00	35.12	0.35
TS-00010-4-3	579.61	2028.73	5042.58	797.82	1048.32	85.19	21.12	3730.39	4.34	2.87	5.20	148.62	62.69	2.26	0.29	0.00	47.79	2.33
TS-00010-3A	1002.65	3087.96	5677.97	719.15	2835.79	84.37	20.43	5479.49	3.85	2.56	3.17	353.69	61.82	2.16	0.24	0.02	73.72	1.65
TS-00010-4-1	593.34	1946.78	5564.40	794.08	1034.17	85.52	19.29	2544.41	2.57	2.47	4.49	68.43	59.69	2.13	0.24	0.02	22.72	2.53
TS-00010-1A	384.47	2357.89	2887.21	250.88	1496.95	85.20	19.38	3544.71	2.79	2.01	1.43	268.56	55.71	2.16	0.15	0.09	15.65	0.62
TS-00010-4-4	721.32	1632.35	5948.94	903.50	873.18	87.34	21.57	3314.51	5.06	2.65	4.14	26.76	54.50	2.31	0.27	0.02	26.88	2.07
TS-00011-4A	226.78	449.20	1040.23	25.64	608.37	143.77	51.08	7098.69	90.99	27.88	0.12	157.74	9.48	1.96	0.29	0.01	0.82	0.82
TS-00011-2-3	221.40	466.50	1974.73	80.34	976.17	93.65	112.03	17784.68	137.37	37.62	0.34	313.78	9.20	1.23	0.68	0.00	1.44	0.45
TS-00011-1-4	203.99	431.16	164.16	1.67	1249.57	91.97	109.88	19010.77	139.84	37.46	0.02	280.86	9.07	1.33	0.82	0.00	1.45	0.20
TS-00011-3A	256.25	439.49	161.55	59.05	1338.26	95.41	108.36	18847.44	140.54	37.76	0.19	288.00	9.07	1.25	0.70	0.00	1.49	0.59
TS-00011-1-3	207.73	447.25	311.00	69.23	1581.59	95.84	127.67	19259.07	139.43	37.88	0.05	275.30	8.99	1.14	0.79	0.00	1.56	1.45
TS-00011-2-2	267.69	452.16	785.52	19.23	1640.32	93.20	107.06	18533.51	137.76	36.65	0.16	287.98	8.97	1.17	0.71	0.02	1.43	1.24
TS-00011-1-2	236.78	384.13	809.66	96.32	1134.58	94.01	56.53	18300.01	129.96	35.89	0.29	227.10	8.94	1.05	0.71	0.00	1.42	0.54
TS-00011-3B	133.10	416.55	642.14	11.31	1423.96	95.47	147.65	18487.78	139.07	38.01	0.20	279.38	8.89	1.19	0.78	0.01	1.72	0.82
TS-00011-1-1	977.51	553.17	9461.87	1495.45	917.01	91.71	66.09	13959.51	130.84	36.29	0.97	251.55	8.86	1.24	0.64	0.01	1.64	1.22

Sample ID	Mg (ppm)	Al (ppm)	Si (ppm)	Ca (ppm)	Ti (ppm)	V (ppm)	Cr (ppm)	Mn (ppm)	Co (ppm)	Ni (ppm)	Cu (ppm)	Zn (ppm)	Ga (ppm)	Ge (ppm)	Mo (ppm)	Ag (ppm)	Sn (ppm)	Pb (ppm)
TS-00011-2A	184.71	436.73	447.47	16.26	1476.93	94.02	104.07	17998.10	138.42	37.65	0.19	331.97	8.85	1.03	0.69	0.00	1.54	0.67
TS-00011-2-1	273.04	392.34	1378.78	58.21	1551.05	93.58	92.14	17733.18	138.10	37.17	0.11	227.00	8.79	1.15	0.77	0.00	1.61	0.25
TS-00011-5A	25.38	245.05	155.94	20.32	828.84	125.31	74.66	6480.73	63.46	24.98	0.47	59.60	8.21	1.68	0.27	0.01	1.01	0.57
PA2-10S-43A	11.00	964.00	828.50	180.00	2147.50	259.80	281.90	13825.00	5.91	1.82	0.07	256.55	0.52	0.25	0.03		0.03	0.03
PA2-10S-44A	11.00	662.25	2408.00	180.00	1543.00	245.05	285.00	8630.00	5.38	1.83	0.07	174.40	0.52	0.25	0.03		0.03	0.03
J_PA1-1-28A	69.90	737.00	405.00	245.00	245.90	42.71	9.30	1680.00	13.44	2.66	0.11	3.99	2.30	1.29	0.04	0.01	0.30	0.11
J_PA1-1-29A	1353.50	1772.50	2280.00	255.00	279.50	44.04	10.80	3395.00	13.83	3.02	0.28	22.70	2.80	1.40	0.08	0.03	0.50	0.27
J_PA1-1-30A	204.10	1022.00	440.00	255.00	115.60	58.74	3.88	2294.00	6.10	2.03	0.10	11.00	1.54	1.46	0.09	0.01	0.46	0.03
J_PA1-1-31A	281.20	968.00	425.00	230.00	123.80	60.99	13.21	2321.00	9.35	3.45	0.09	8.50	1.59	1.59	0.07	0.03	0.40	0.02
J_PA1-1-32A	507.00	998.00	470.00	240.00	141.40	58.19	8.22	5482.00	16.55	4.68	0.11	15.70	1.56	1.73	0.16	0.01	0.20	0.02
PA2-11S-39A	11.00	691.00	1085.00	180.00	945.00	49.24	30.40	8040.50	1.49	1.53	0.07	52.75	0.52	0.25	0.03		37.45	0.03
PA2-11S-40A	11.00	948.50	320.00	180.00	943.50	48.55	17.85	12135.00	5.68	0.72	0.07	396.60	0.52	0.25	0.03		81.75	0.03
PA2-11S-41A	11.00	812.70	320.00	180.00	868.00	48.67	38.10	12275.00	5.00	1.45	0.07	180.90	0.52	0.25	0.03		58.80	0.03
PA2-11S-42A	11.00	799.50	510.00	180.00	926.50	52.40	30.25	12925.00	4.86	1.06	0.39	109.95	0.52	0.25	0.03		60.40	0.03
J_PA2-1-18A	685.00	7320.00	800.00	130.00	2306.00	124.70	127.40	5950.00	32.50	40.00	0.07	160.00	18.07	4.04	1.22	0.01	1.84	0.18
J_PA2-1-19A	488.00	5720.00	380.00	195.00	1984.00	108.70	111.20	5069.00	29.34	36.00	0.11	106.00	16.30	3.39	0.86	0.02	1.64	0.66
J_PA2-1-20A	387.00	4380.00	300.00	195.00	1858.00	112.50	120.70	3880.00	25.91	29.43	0.28	57.70	15.39	3.64	0.37	0.02	1.52	0.21
J_PA2-1-21A	536.00	5050.00	390.00	180.00	2012.00	115.90	62.00	5090.00	26.69	30.30	0.12	131.60	16.04	3.60	0.97	0.01	1.60	0.07
J_PA2-1-22A	387.30	4182.00	390.00	180.00	1838.00	109.50	64.40	4380.00	22.60	27.10	0.11	36.60	14.51	3.32	0.36	0.02	1.45	0.25
J_PA2-1-23A	557.00	4680.00	395.00	215.00	1853.00	110.60	125.40	4600.00	23.00	24.82	0.23	75.50	15.64	3.50	0.54	0.01	1.58	0.11
TS-00033-4A	505.50	7507.67	1658.37	102.90	6504.90	130.69	3.59	852.53	9.48	0.69	0.59	820.35	195.95	6.24	33.74	0.25	174.83	0.58
TS-00033-2-2	151.71	5968.29	738.91	134.21	9256.92	106.72	3.99	1003.44	8.07	0.56	0.56	482.01	192.76	5.65	34.87	0.21	169.77	0.67

Sample ID	Mg (ppm)	Al (ppm)	Si (ppm)	Ca (ppm)	Ti (ppm)	V (ppm)	Cr (ppm)	Mn (ppm)	Co (ppm)	Ni (ppm)	Cu (ppm)	Zn (ppm)	Ga (ppm)	Ge (ppm)	Mo (ppm)	Ag (ppm)	Sn (ppm)	Pb (ppm)
TS-00033-2-1	756.30	7184.94	4609.76	138.01	2353.65	97.63	5.56	357.44	7.81	0.70	0.45	304.40	188.21	5.85	36.23	0.30	65.32	0.68
TS-00033-2A	584.80	5874.04	3215.40	221.69	4516.32	106.32	4.85	629.39	6.67	0.71	1.66	428.15	183.32	5.90	6.26	0.25	106.98	0.99
TS-00033-3-3	336.64	4561.42	2201.13	70.42	3693.43	97.44	2.46	414.25	7.34	0.45	0.48	238.30	170.37	6.77	34.10	0.09	69.31	1.21
TS-00033-3-1	497.23	3844.70	3235.71	282.01	2615.07	98.34	7.90	475.43	7.13	0.66	0.81	174.60	164.13	6.42	37.46	0.08	61.80	0.64
TS-00033-1A	376.07	5223.03	2035.06	111.66	2437.81	105.78	1.39	470.04	7.54	0.61	0.31	338.04	161.58	5.74	36.00	0.10	43.13	0.67
TS-00033-3-4	478.67	3817.98	3599.42	177.90	1758.68	100.65	1.44	302.19	6.49	0.39	0.60	187.31	148.83	6.72	41.05	0.41	40.59	1.61
TS-00033-3-5	387.84	3492.66	2749.86	301.99	3299.25	91.02	4.15	509.26	5.50	0.86	3.75	699.41	144.78	5.68	27.63	1.23	54.46	1.54
PA2-SEM8-45A	11.00	684.60	908.00	180.00	220.85	41.40	5.21	4440.50	7.70	2.04	0.54	28.00	0.52	0.25	0.24		1.62	0.03
PA2-SEM8-46A	11.00	974.50	970.00	180.00	353.50	19.54	5.25	8468.50	10.63	2.18	0.07	6.40	0.52	0.25	0.51		2.12	0.03
PA2-SEM8-47A	11.00	858.00	453.00	180.00	228.70	66.20	12.30	7307.00	4.92	1.06	0.07	166.00	0.52	0.25	0.34		1.56	0.03
TS-00019-1A	752.45	6547.44	396.34	33.47	4096.56	44.57	14.16	5943.76	6.80	3.44	0.10	215.70	37.30	4.20	0.26	0.02	6.10	0.47
TS-00019-5-4	243.99	1355.83	1013.05	169.82	406.53	42.52	12.07	1488.67	12.08	5.12	0.02	13.38	32.28	2.92	0.11	0.00	1.04	0.10
TS-00019-6-1	1340.78	3599.16	2718.99	113.23	500.85	35.76	13.91	2005.12	11.41	5.62	0.19	66.83	30.37	2.37	0.17	0.00	3.50	0.17
TS-00019-5-1	920.25	3854.73	2510.19	5.88	2415.17	40.70	18.69	4170.96	14.58	5.19	0.12	50.38	28.88	2.64	0.22	0.02	2.71	0.13
TS-00019-6A	702.36	2740.56	1710.20	75.64	1408.81	35.98	14.03	3001.91	12.92	5.17	0.29	96.70	28.25	2.77	0.35	0.02	3.74	0.25
TS-00019-3A	822.82	3307.47	3590.35	158.10	1736.52	37.66	10.20	3542.68	8.78	4.70	0.83	148.68	24.95	3.46	0.16	0.19	1.93	0.42
TS-00019-2A	439.73	1940.27	1448.25	67.13	514.26	39.34	15.31	2227.94	7.75	3.66	0.12	20.91	24.71	3.33	0.14	0.01	2.11	0.14
TS-00019-5-3	1154.12	2038.33	2453.03	73.02	603.59	21.59	20.12	1782.54	11.31	4.77	0.10	16.24	24.63	1.95	0.09	0.00	1.21	0.11
TS-00019-3-3	453.47	1642.59	1547.53	82.42	2062.30	37.77	7.69	3717.03	8.21	4.72	0.70	268.67	24.11	3.59	0.16	0.11	2.10	0.60
TS-00019-4A	292.01	2336.20	614.23	77.13	376.47	42.33	26.68	2269.21	9.89	4.83	0.05	28.81	23.70	3.39	0.10	0.00	2.56	0.15
TS-00019-3-4	548.51	1587.79	1633.06	37.12	1984.75	37.50	9.35	3617.65	7.91	4.29	0.21	15.21	23.05	3.54	0.21	0.03	1.82	1.95
TS-00021-4A	761.80	4986.07	803.40	155.58	1779.91	147.16	90.27	3026.73	41.17	46.54	0.10	128.82	25.97	5.15	0.71	0.00	4.31	0.34

Sample ID	Mg (ppm)	Al (ppm)	Si (ppm)	Ca (ppm)	Ti (ppm)	V (ppm)	Cr (ppm)	Mn (ppm)	Co (ppm)	Ni (ppm)	Cu (ppm)	Zn (ppm)	Ga (ppm)	Ge (ppm)	Mo (ppm)	Ag (ppm)	Sn (ppm)	Pb (ppm)
TS-00021-2-4	891.61	5633.14	949.40	94.33	3409.94	170.57	173.49	4924.33	43.93	48.10	0.90	270.57	25.87	5.88	0.59	0.02	3.84	1.06
TS-00021-1-4	890.40	5647.15	696.46	106.68	3640.57	147.52	181.28	4659.58	41.86	46.12	1.39	186.63	24.80	4.76	0.56	0.00	4.05	0.32
TS-00021-1-2	870.00	5229.22	518.62	50.03	6513.44	144.53	163.81	5966.73	41.74	45.90	0.39	331.92	24.59	4.86	0.48	0.00	4.95	0.47
TS-00021-2A	899.43	5758.44	1469.46	136.21	1798.50	166.18	152.44	2611.75	43.78	47.31	1.06	579.35	24.15	5.04	0.47	0.00	3.49	0.81
TS-00021-3A	867.84	4494.18	860.41	575.89	1048.08	150.74	137.15	2096.28	39.16	46.85	0.19	174.31	23.85	4.97	0.52	0.01	3.09	0.45
TS-00021-1-3	594.03	4543.31	1391.22	199.73	1541.82	143.17	30.21	2931.71	37.59	44.40	0.30	88.17	23.59	4.40	0.35	0.00	3.99	0.40
TS-00021-2-3	1513.68	4646.68	1895.56	49.11	1836.57	167.28	101.59	2587.54	38.43	47.64	0.10	143.49	23.07	4.80	0.23	0.00	2.84	0.60

Lihtlitsents lõputöö reprodutseerimiseks ja üldsusele kättesaadavaks tegemiseks

Mina, AlvarRatt,

(autori nimi)

1. annan Tartu Ülikoolile tasuta loa (lihtlitsentsi) minu loodud teose

   Composition of magnetite trace elements in the Jõhvi magnetic quartzite in north-east Estonia as an indicator of iron mineralisation processes,

   (lõputöö pealkiri)

   mille juhendajad on Kalle Kirsimäe ja Siim Nirgi,

   (juhendaja nimi)

   reprodutseerimiseks eesmärgiga seda säilitada, sealhulgas lisada digitaalarhiivi DSpace kuni autoriõiguse kehtivuse lõppemiseni.

2. Annan Tartu Ülikoolile loa teha punktis 1 nimetatud teos üldsusele kättesaadavaks Tartu Ülikooli veebikeskkonna, sealhulgas digitaalarhiivi DSpace kaudu Creative Commonsi litsentsiga CC BY NC ND 4.0, mis lubab autorile viidates teost reprodutseerida, levitada ja üldsusele suunata ning keelab luua tuletatud teost ja kasutada teost ärieesmärgil, alates ***27.05.2024*** kuni autoriõiguse kehtivuse lõppemiseni.

3. Olen teadlik, et punktides 1 ja 2 nimetatud õigused jäävad alles ka autorile.

4. Kinnitan, et lihtlitsentsi andmisega ei riku ma teiste isikute intellektuaalomandi ega isikuandmete kaitse õigusaktidest tulenevaid õigusi.

Alvar Ratt

27.05.2024